

Post-Processing Synchronized Bistatic Radar for Long Offset Glacier Sounding

Nicole L. Bienert¹, Member, IEEE, Dustin M. Schroeder², Senior Member, IEEE, Sean T. Peters³, Member, IEEE, Emma J. MacKie, Graduate Student Member, IEEE, Eliza J. Dawson, Matthew R. Siegfried⁴, Member, IEEE, Rohan Sanda, and Poul Christoffersen

Abstract—Radar tomography of glaciers promises to improve imaging and estimates of subsurface ice-sheet structures and properties, including temperature distributions, basal materials, ice fabric, and englacial water content. However, bistatic radar data with long (i.e., larger than the ice thickness) walk-away surveys are required to constrain high-fidelity tomographic inversions. These long-offset data have proven difficult to collect due to the hardware complexity of existing synchronization techniques. Therefore, we remove the hardware complexity required for real-time synchronization by synchronizing in postprocessing. Our technique transforms an Autonomous phase-sensitive Radio Echo Sounder (ApRES) system and a software-defined radio receiver into a coherent bistatic radar capable of recovering basal echoes at long offsets. We validated our system at Whillans Ice Stream, West Antarctica, with a walk-away survey up to 1300 m (797 m thick) and at Store Glacier, Greenland, up to 1450 m (1028 m thick). At both field sites, we measured the basal echo at angles beyond the point of total internal reflection (TIR), whose previous literature had set as a hard physical limit. We support our experimental results with high-frequency structure simulation, which shows that ground-based radar systems capture evanescent waves and are not hindered by TIR. Our analysis and experiments demonstrate a system capable of executing wide-angle bistatic radar surveys for improved geometric and radiometric resolution of inversions for englacial and subglacial properties.

Index Terms—Bistatic radar, bistatic tomography, direct-path synchronization, ice-antenna coupling, phase alignment, radio echo sounder, signal-to-noise ratio (SNR) gain, summation noise statistics.

Manuscript received October 13, 2021; revised December 22, 2021; accepted January 25, 2022. Date of publication January 27, 2022; date of current version March 17, 2022. The work of Nicole L. Bienert was supported in part by the NSF Division of Graduate Education (DGE) under Grant 1656518 and in part by the NASA Cryospheric Sciences Program under Grant NNX16AJ95G. The work of Dustin M. Schroeder was supported by the NASA Cryospheric Sciences Program under Grant NNX16AJ95G. The work of Sean T. Peters, Emma J. MacKie, Eliza J. Dawson, and Poul Christoffersen was supported by the European Research Council through the European Union's Horizon 2020 Research and Innovation Program under Grant 683043. The work of of Matthew R. Siegfried was supported by NSF under Grant 1543441. (Corresponding author: Nicole L. Bienert.)

Nicole L. Bienert, Sean T. Peters, and Rohan Sanda are with the Department of Electrical Engineering, Stanford University, Stanford, CA 94305 USA (e-mail: bienert@stanford.edu).

Dustin M. Schroeder is with the Department of Electrical Engineering and the Department of Geophysics, Stanford University, Stanford, CA 94305 USA.

Emma J. MacKie and Eliza J. Dawson are with the Department of Geophysics, Stanford University, Stanford, CA 94305 USA.

Matthew R. Siegfried is with the Department of Geophysics, Colorado School of Mines, Golden, CO 80401 USA.

Poul Christoffersen is with the Department of Geography, University of Cambridge, Cambridge CB2 1ER, U.K.

Digital Object Identifier 10.1109/TGRS.2022.3147172

NOMENCLATURE

Material Properties:

α	Attenuation coefficient (Np/m).
N_a	Attenuation loss, one-way depth averaged (dB/km).
a	Attenuation loss, two-way attenuation as a scalar.
$\tan \delta$	Loss tangent.
ϵ	Permittivity (F/m).
ϵ''	Imaginary part of permittivity (F/m).
ϵ'	Real part of permittivity (F/m).
ϵ_r	Real relative permittivity ϵ'/ϵ_0 (e.g., ice ~ 3.18).
ϵ_0	Permittivity of free space (8.853×10^{-12} F/m).
μ_0	Permeability of free space ($4\pi \times 10^{-7}$ H/m).
σ	Static conductivity of ice, excluding $\omega\epsilon''$ (S/m).
σ_s	Static conductivity (S/m).
σ_n	Static conductivity of a grid space n (S/m).
σ_i^0	Molar conductivity of a compound i (S/m).

Standard Deviation:

$\bar{\sigma}_v$	Standard deviation of noise voltage before processing.
$\bar{\sigma}_{\text{noise PW}}$	Standard deviation of noise power after processing.

Signal:

$v_{\text{TX}}(t)$	Transmitted voltage signal (V).
$v(t), v_m(t)$	Voltage signal of echo before processing (V).
$s(t)$	Voltage signal of echo after processing (V).
V	Voltage peak of matched filtered signal (V).
b_m	Power received for measurement m , normalized to remove dependence on vars other than conductivity.

Noise:

W	White Gaussian noise random variable (V).
$w(t)$	White Gaussian noise voltage before processing (V).
$n(t)$	Noise voltage after processing (V).

Radar Equation:

P_{RX}	Power received by radar (W).
P_{TX}	Power transmitted by radar (W).
G_{TX}	Transmitting antenna gain for a particular angle.
G_{RX}	Receiving antenna gain for a certain angle.
ρ	Scattering loss from basal roughness.

- Γ Reflection coefficient for electric/magnetic field squared for operating on power.
 θ Angle: indicates angular dependence of variables.
 θ_i Incidence angle between wave and surface normal.
 θ_t Transmission angle between wave and surface normal.

EM Properties:

- λ Wavelength in ice (m).
 c Speed of light (m/s).
 ω Angular frequency (rad·s⁻¹).
 η Intrinsic impedance of medium for EM wave (Ω).
 t Time (s).
 d Path length: total distance the wave travels (m).
 τ Chirp length (s).
 B Bandwidth (Hz).
 ϕ Phase shift of voltage/electromagnetic wave.
 ϕ_m Random phase shift of a signal caused by the difference in the TX and RX local oscillators.
 ϕ_b Propagation phase shift of wave reflected from bed.
 ϕ_d Propagation phase shift of wave that traveled along the direct path through the air between TX and RX.

Misc:

- C_m Concentration of compound m (mol/L).
 E_m^0 Activation energy (eV).
 E_{TX} Energy in transmitted signal (J).
 \vec{E} Electric field (V/m).
 \vec{H} Magnetic field (A/m).
 h Ice thickness (m).
 R Resistance (Ω).
 k Boltzmann's constant (8.617×10^6 eV/K)
 also used as degrees of freedom for χ^2 distribution.
 T Temperature (K).
 T_r Reference temperature for chemistry measurements (K).
 t_0 Time the chirp was transmitted (s).
 t_b Time the basal echo was received (s).
 t_d Time the direct path was received (s).
 x Antenna separation between transmitter and receiver (m).
 N Number of chirps summed.

I. INTRODUCTION

ICE penetrating radar sounding is a widely used and information-rich geophysical technique that is a foundational tool for terrestrial and planetary glaciological studies [1]. Monostatic nadir-facing records of radar echo strengths collected from airborne and ground-based platforms have been variously exploited to observe and interpret subglacial hydrology [2], [3], basal thermal state [4], ice fabric [5], [6], englacial temperature [7], debris [8], and water [9]. In many of these studies, researchers exploited the temperature dependence of englacial attenuation [10] and/or basal reflectivity [11] to infer subglacial [12] or englacial temperatures [13] or thermal anomalies [14]. Despite their wide application and utility, these monostatic approaches suffer ambiguity in their

attenuation/reflectivity signals [15] and do not achieve the radiometric or geometric resolution of array-based [16] or tomographic [17] approaches. However, bistatic and tomographic ice-penetrating radar sounding systems and studies remain rare.

Tomography is a powerful tool that creates estimates of the 2-D distribution of subsurface properties using attenuation and/or time of flight data. A wide diversity in transmitter–receiver offsets is particularly important for constraining inversions and limiting the solution space [18]–[21]. Well-constrained inversions require the constraints provided by longer offsets. Applying tomographic and variable-offset approaches to ice-penetrating radar data enables investigating glaciological processes (e.g., shear margin thermal anomalies [22], [23]) that fall below the radiometric and geometric resolution of most monostatic radar sounding inversions.

A handful of bistatic radar experiments have been working toward the large offsets required for well-constrained tomographic inversions. For example, Drews *et al.* [24] used a common shot configuration to measure radar-wave travel time and invert for the ice density profile as a function of depth on roughly 400-m-thick ice shelves. Another investigation constrained the water content at various depths inside a shallow alpine glacier using the wave speed measured in a common midpoint (CMP) experiment [25]. Other investigations have favored measuring attenuation to invert for subsurface properties. For example, Winebrenner *et al.* [26] employed a CMP survey to collect bed echo power at varying offsets and accurately solved for both the depth-averaged attenuation and conductivity. Holschuh *et al.* [27] extended this analysis by including englacial layer reflectors to estimate depth-averaged ice attenuation to a particular depth of reflector. While these investigations estimated ice properties in one dimension, their use of a bistatic configuration showed promise for bistatic tomography. To obtain accurate 2-D tomographic inversions [18]–[21], bistatic radars must reach larger antenna separations than those used in these studies.

The largest antenna separation achieved in the literature was around 1000 m, and the authors reported that wide-angle radar surveys are impossible due to total internal reflection (TIR) [27]. TIR occurs when the transmission angle of a wave passing through an interface exceeds 90° and the waves travel along the ice surface as evanescent waves rather than passing through the medium [28]. The critical incidence angle beyond which this phenomenon can occur is given by Snell's law and only occurs when a wave travels from a medium with higher refractive index to a lower one. This phenomenon can prevent a wave from exiting the ice and being detected by the receiving antenna. We hypothesize that TIR is only a barrier to airborne experiments and does not limit ground-based systems. We test this in high-frequency structure simulator (HFSS) and experimentation. The next challenge is overcoming signal attenuation at large antenna separations, which in past experiments caused poor signal-to-noise ratio (SNR) that limited previous systems and experiments [24], [27].

Weak signals can be amplified above additive noise through coherent summation, which requires synchronization, or the time and phase alignment of chirps in either hardware or

software. While incoherent summation, the summing of powers, can be applied to phase unsynchronized data, it only provides an SNR gain of \sqrt{N} , where N is the number of chirps summed. The square root taper in SNR gain makes unsynchronized wide-angle surveys intractable for radioglaciology. Adding phase-aligned voltage waveforms, called coherent summation, offers N SNR gain but requires phase synchronization to prevent destructive interference from phase misalignment caused by local oscillator (LO) drift. Traditional monostatic radar systems are synchronized in hardware, but this does not extend to long-offset bistatic measurements due to radio frequency cable losses. While a fiber-optic link could be used, the length of cable required would be cumbersome and impractical in field deployments; therefore, we pursue wireless synchronization.

Several wireless synchronization methods exist that use a separate channel to transfer transmit time and phase information between transmitters and receivers. Many methods synchronize daughter clocks to the mother using techniques such as timing signals sent by the master [29], [30] and response delay between daughter and mother nodes [31]. Other techniques [32]–[34] not only provide timing synchronization of clocks but also eliminate phase drift of LOs to enable coherent summation of chirps in radar applications. All these approaches use a synchronization channel separate from the radar. Consequentially, systems using active synchronization techniques either reduce radar pulse repetition frequency (PRF) to intertwine synchronization signals or use a separate antenna at a different frequency for the synchronization channel. The former option reduces data collection efficiency and the latter increases hardware complexity. These are not significant challenges for bistatic radar tomography of glaciers; however, in our pursuit of a simple, low-cost system for glaciology, we developed a new type of synchronization that trades these issues for increased data volume and post-processing time.

For applications that do not require real-time synchronization, we introduce a postprocessing synchronization approach that does not necessitate a reduced PRF and additional hardware. Rather than use a separate channel to communicate transmit time and phase information, we extract this information directly from the radar data. In radar data, before any echoes bounce back to the receiver, a wave is recorded, which travels the shortest path between the transmitter and the receiver. This direct path is typically discarded, but we use this high SNR signal to extract the transmit phase and transmit time information and use it to synchronize received chirps. While the passive synchronization concept has the potential to reach 100% duty cycle, our implementation optimizes for usability and low cost, so we reduce our net PRF to accommodate the write speed capability of lower cost software-defined radios (SDRs). As the cost of capable hardware comes down, future iterations may reach 100% duty cycle to minimize the time scientists spend conducting experiments out in the cold.

We implement our processing-based synchronization technique on data collected by an Ettus Research E312 SDR that passively measured Autonomous phase-sensitive Radio Echo Sounder (ApRES) [35] chirps at increasing offsets.

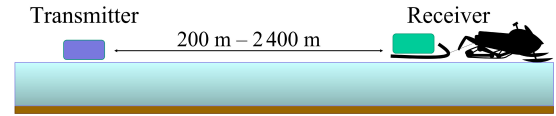


Fig. 1. Our experimental configuration included a transmitter and receiver spatially separated by 200–2400 m. The transmitter was always static, while the receiver was static in some tests and slowly moving in others.

We validated our system at Whillans Ice Stream, Antarctica, where we recovered basal echoes at the static offsets of 300, 600, 900, and 1300 m. Experiments show that our system synchronizes the data sufficiently to attain N processing gain from coherently summing N chirps, matching theory. We extend this experiment at Store Glacier, Greenland, where we conducted a walk-away experiment and recovered basal echoes up to 1450 m, beyond the point of TIR. This experiment is depicted in Fig. 1. The results suggest that basal echoes can be recovered from additive noise at any antenna separation provided a detectable direct path.

II. METHODS

A. Electromagnetic Simulation

To explore the fundamental limits of offsets achievable and exploitable by our new system, we simulated our experiment in HFSS to assess whether TIR limits the maximum antenna separation. We simulated a plane wave propagating in ice, impinging on a flat air–ice interface and measured how much power was received by a dipole antenna above the ice–air interface. We simulated isotropic ice with a relative permittivity (ϵ_r) of 3.18, a loss tangent ($\tan \delta$) of 0.0062 [36], and a conductivity (σ) of 1×10^{-5} S/m, consistent with [10]. An incident plane wave excitation was assigned to the bottom of the ice and perfectly matched layer (PML) boundaries are applied to all other exposed sides of the simulation. In terms of wavelength (λ), the simulation area was roughly $15\lambda \times 11\lambda \times 1.5\lambda$ with the antenna at minimum $\lambda/2$ from PML boundaries. A dipole antenna was suspended in air just above the ice, the design of which we parametrically optimized in HFSS. The dipole antenna was represented by two perfectly conductive cylinders of length 45 cm with a gap of 0.749 cm and a radius of 0.749 cm, which was found to have better than -15 -dB return loss at 300 MHz for both distances from the ice. Note that the ice slightly tunes the antenna depending on the proximity of the antenna to the ice. The voltage received by the antenna was calculated by integrating the tangent electric field between the cylinders using the fields calculator as explained in [37].

B. Experiment

We developed and demonstrated a bistatic system that can detect a basal reflection with large transmitter–receiver separation. We used an ApRES [35] as our transmitter and an Ettus Research E312 SDR as our receiver. The individual hardware used for the transmitter and receiver is incoherent from each other, so we created a coherent system by exploiting the signal direct path to synchronize the devices. We conducted validation testing at Whillans Ice Stream, West Antarctica, using static transmitter–receiver separations of 300, 600, 900,

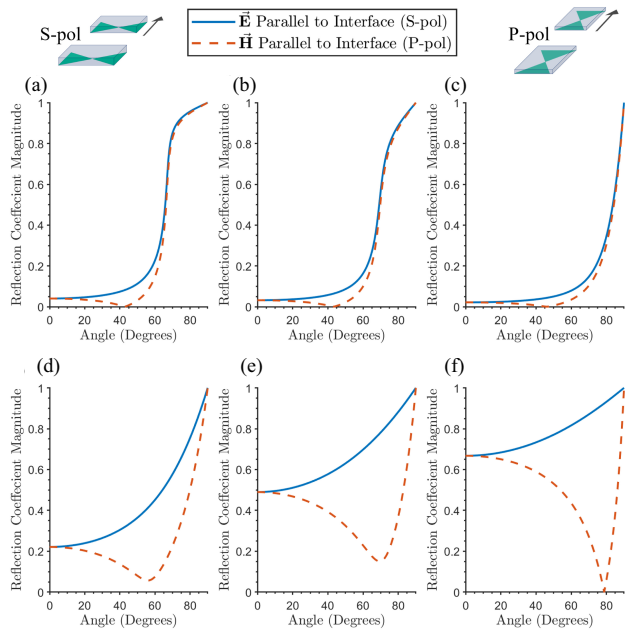


Fig. 2. Theoretical reflectivity as described in Appendix A-A is plotted above, which shows that reflected power depends on antenna orientation, off-nadir bistatic angle, and basal material. A wave with the electric field (\vec{E}) parallel to the bed (blue line) has a significantly higher reflection coefficient than its orthogonal counterpart (\vec{H} , red dashed line) for all bed types. This result drives the orientation of antennas with respect to the transect in our field demonstrations. The electrical properties used for ice were $\epsilon_r = 3.18$ $\tan \delta = 0.0062$ and the basal properties are as follows [36]. (a) $\epsilon_r = 2.7$ $\tan \delta = 0.022$ (frozen bedrock). (b) $\epsilon_r = 2.8$ $\tan \delta = 0.035$ (frozen till). (c) $\epsilon_r = 3.43$ $\tan \delta = 0.05$ (marine ice). (d) $\epsilon_r = 6.6$ $\tan \delta = 0.41$ (unfrozen bedrock). (e) $\epsilon_r = 18$ $\tan \delta = 0.82$ (unfrozen till). (f) $\epsilon_r = 80$ $\tan \delta = 0.002$ (fresh water).

and 1300 m. Measurements were conducted along the transect between the static transmitter position at 84.24892°S and 153.91115°W and the maximum receiver position 84.25877°S and 153.97427°W. At Store Glacier, Greenland, we conducted a walk-away survey along the transect between 70.557821°N and 50.091945°W and 70.57078°N and 50.0429817°W. As an on-foot experiment, we restricted the maximum antenna separation to 2300 m to prevent overexertion. This moving experiment included a record of the static transmitter location using a global navigation satellite system (GNSS) receiver and a periodic recording of the GNSS location of the radar receiver, embedded in the radar data. Antennas were always oriented facing the ice with the electric field parallel to the bed (s-pol), as shown in Fig. 2. Orienting the antennas in h-pol causes power loss due to the orientation dependence of the reflection coefficient. We provide full instructions for repeating our experiment at [38] and the dataset is available at [39].

C. Hardware

Our system consists of the transmitter and receiver depicted in Fig. 3. Both the transmitter and the receiver were connected to a cavity-backed bowtie antenna with a gain of 6.56 dBi across a bandwidth of 200–400 MHz. The peak antenna gain occurs at nadir; however, the antenna has a large beamwidth of 115°, allowing detection of the direct path and basal echoes at long offsets. The ApRES was used as the transmitter because our field-going collaborators use these systems, but

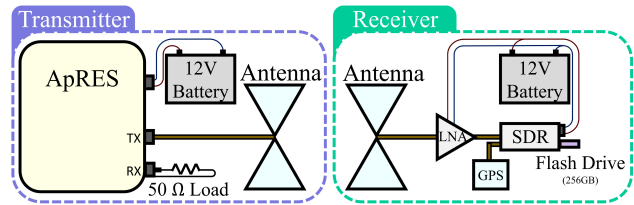


Fig. 3. Transmit and receive chains are shown. Here, we use an ApRES as the FMCW transmitter, although any chirped transmitter could be used instead. The receive chain includes a bowtie antenna and low noise amplifier external to the SDR, with internal components including amplifiers, bandpass filters, and an IQ analog-to-digital converter.

we intend to develop an option for an SDR transmitter for more control over the transmitted waveform. The receive chain included a low noise amplifier from Advanced Receiver Research, providing 20-dB gain and a 0.5-dB noise for 300–360 MHz. The transmitter emits a 20-dBm stable linear frequency-modulated continuous-wave (LFMCW) chirp that ramps from 200 to 400 MHz over a 1-s chirp length. The ApRES transmits continuously (100% duty cycle), while the SDR records time-domain data in 8-s segments, delineated by downtime for data transfer. We programmed the SDR to apply a bandpass filter (323–338 MHz) and 62 dB of gain, which is the highest gain that still minimizes amplifier nonlinearities.

Due to write speed limitations of USB 2.0 and our choice to use an 8-s chirp, we are unable to achieve the maximum 56-MHz in-phase quadrature (IQ) sampling rate of the SDR. We chose a reduced bandwidth and IQ sampling rate of 15.3 MHz centered at 330 MHz and a long chirp of 1 s to balance the increased SNR provided by longer chirps (see Appendix B-E and the increased interference of overlapping sinc functions caused by lower bandwidths (see Section A-B2)). As shown in Appendixes A-B1 and B-E, bandwidth does not influence the SNR of an isolated chirp and therefore was not considered in the tradeoff.

D. Processing

To recover basal echoes at long offsets without the use of an active synchronization channel, we implement a novel direct-path synchronization processing chain in MATLAB. As shown in Fig. 4, our processing chain is split into three phases, each summarized in the following. We provide our GitHub repository at [38].

Phase 1: The GNSS position of the receiver is extracted from the last 100 bytes of each 8-s recording stored by the SDR to determine the precise offset from the transmitter. Next, we matched filter each time-domain recording with a reference transmit signal to improve the SNR. The cross correlation peaks at the time the direct path is received (Fig. 4). The matched filtered output is then cropped around this peak, separating individual chirps. Clipped chirps that occurred in between SDR recordings are then removed.

Phase 2: We estimate the direct-path delay with subsample resolution using quadratic least-squares peak estimation, as discussed in [31] and [32]. This approach to pinpointing the peak at subsample resolution is more data volume efficient than sinc interpolation. The method fits a parabola to the three points at the peak of the discrete signal and finds the analytical

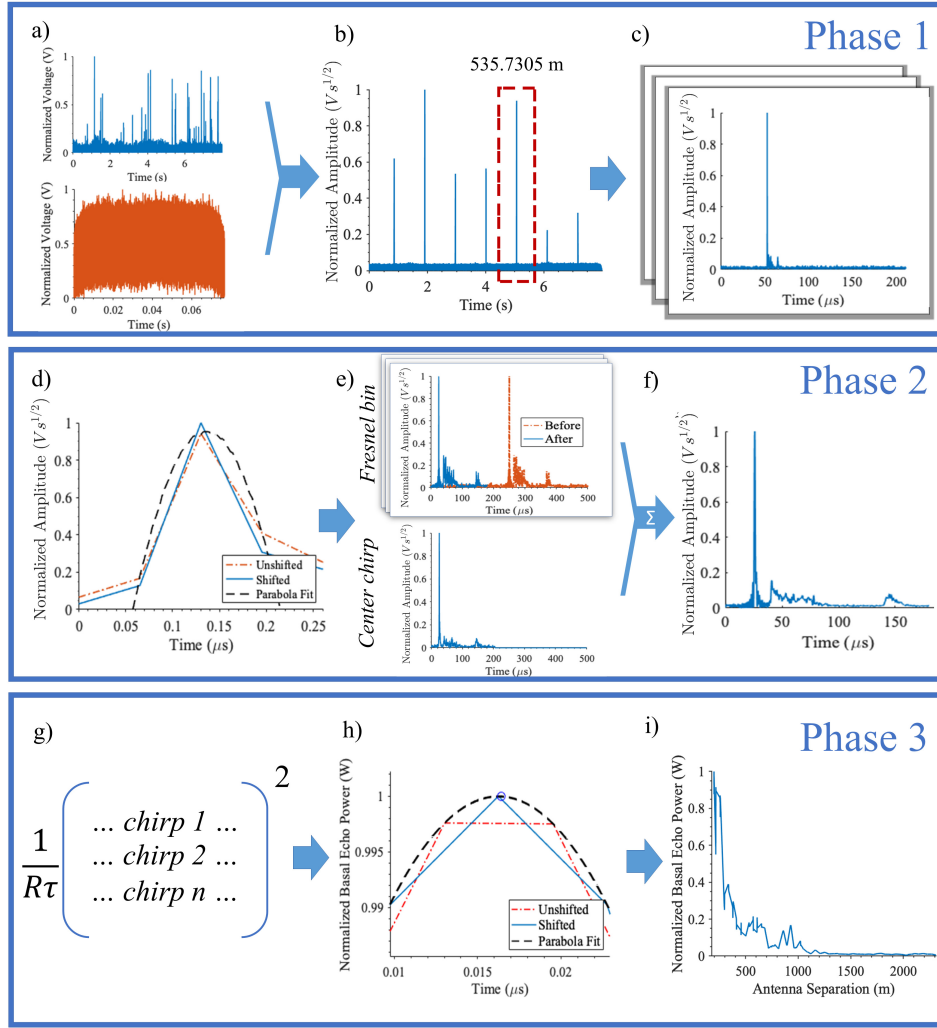


Fig. 4. We illustrate the three-phase processing chain using the chirp received at 537.7 m in Greenland as an example. (a) Reference chirp (red) and a raw 8-s time-domain signal (blue line) are (b) matched filtered to produce the output. The matched filtered output is cropped around each cross correlation peak (red dashed box), which indicates the direct path of a received chirp. (c) Coarse time and phase alignment are applied. (d) Phase 2 first applies quadratic least-squares peak estimation to the direct path. Next, we iterate through each chirp, time-aligning adjacent chirps that reflected from the bed in the same first Fresnel zone as the center chirp. (e) Original chirp (red) is shifted left (blue) to align with the center chirp. (f) Finely time-aligned chirps are then rephased aligned and coherently summed, clearly revealing the bed echo. In Phase 3, (g) we convert the chirp amplitudes to power and (h) again apply quadratic least-squares peak estimation to recover the bed echo power. (i) Bed echo powers are recorded and saved.

parabola maximum. If k_0 represents the time (in samples) of the direct-path peak in discrete signal $s[k]$, then the estimated delay sample k_{delay} can be found

$$k_{\text{delay}} = k_0 - \Delta k$$

$$\Delta k = \frac{s[k_0 + 1] - s[k_0 - 1]}{2 * s[k_0 - 1] - 4 * s[k_0] + 2 * s[k_0 + 1]}. \quad (1)$$

The parabolic fit does not accurately estimate the amplitude of the peak, so we resample the signal in step with k_{delay} to accurately capture the direct-path peak. Resampling is completed in the frequency domain as

$$s[k - \Delta k] = \mathcal{F}^{-1}(\mathcal{F}(s[k])e^{-j2\pi f \Delta k / f_s}). \quad (2)$$

The code then performs the following steps on each corrected chirp i (shown in Fig. 4).

1) Chirp i is upsampled, cropped, and time-aligned with a template waveform using the direct-path peak.

- 2) We create a bin containing all chirps that are reflected from the bed within the first Fresnel zone of chirp i .
- 3) Each bin chirp is upsampled and cropped.
- 4) The direct-path phase ($\phi_d + \phi_m$) is extracted from each bin chirp, and then, each chirp is multiplied by $e^{-j(\phi_d + \phi_m)}$ for phase alignment, as discussed in Section III.
- 5) We use a normalized matched filter to identify bin chirps with low cross correlation with chirp i and omit these from the bin.
- 6) All chirps in the bin are coherently averaged.

Phase 3: The coherently averaged chirp amplitudes are first converted to power in watts from units of $V_s^{(1/2)}$ by squaring, dividing resistance, and dividing by chirp length. Next, we improve the accuracy of the basal power estimation by identifying peak location with quadratic least-squares estimation and resample the waveform to that peak. We then remove bed picks that appear at a depth discontinuous from

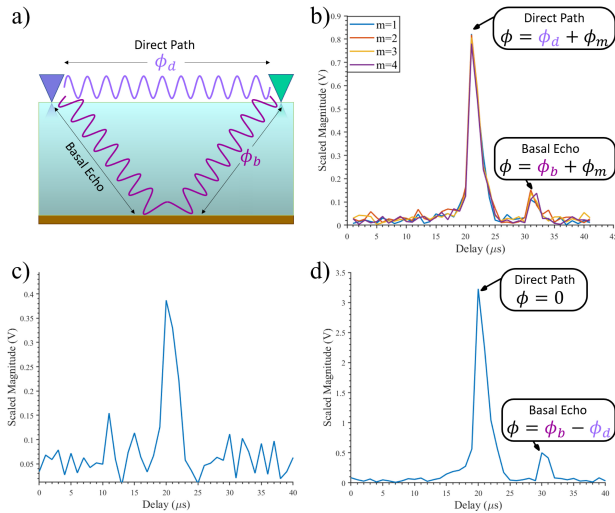


Fig. 5. (a) Wave traveling through the air, called the direct path accumulates a phase shift of ϕ_d . The wave that reflects off the bed gains a phase shift of ϕ_b . (b) Plot of four received chirps after matched filtering. Both the direct path and bed echo have an unknown phase shift, ϕ_m , caused by LO mismatch which changes for each received chirp. (c) Without phase aligning the chirps to remove ϕ_m , the chirps may destructively interfere when complex summed. (d) Each receive chirp is multiplied by $e^{-j(\phi_d + \phi_m)}$ to remove the unknown ϕ_m before coherent summation. The four chirps summed here are from 2018 Store Glacier data using 1-MHz bandwidth and an Ettus B205mini.

surrounding data points. Finally, we estimate the ice depth at each chirp's GPS location. The basal echo powers and estimated ice depths are then saved and can be used for further analysis.

III. PROCESSING-BASED SYNCHRONIZATION

Rather than require a separate synchronization channel to enable coherent summation, we recover relative transmit phase information from the direct-path wave and use it to synchronizing waveforms in phase 2, step 4 of the full processing chain. The received chirp has a random, unknown phase shift from the reference chirp caused by phase offset between transmit and receive LOs (ϕ_m). In addition to this unknown phase, the wave that reflects off the bed accumulates a phase shift of $(2\pi/\lambda)d$ as it propagates a distance d and a phase shift from reflection at the bed for a total shift of ϕ_b , as shown in Fig. 5(a). The wave that takes the shortest path through the air between the transmitter and receiver, called the direct path, accumulates a phase shift of $\phi_d = (2\pi/\lambda)x$, where x is the tx-rx antenna separation. For a static measurement, ϕ_d and ϕ_b will remain constant, but ϕ_m will change over time. If the received echoes are time-aligned and complexly summed without correcting ϕ_m , the signals may destructively interfere, as shown in Fig. 5(c). We remove the random ϕ_m by first obtaining its value from the direct path. After matched filtering the data, the direct-path peak is detectable with phase $\phi_d + \phi_m$, as shown in Fig. 5(b). For each received chirp, we obtain the phase of the direct-path peak ($\phi_d + \phi_m$) and multiply the entire chirp by its complex conjugate $e^{-j(\phi_d + \phi_m)}$. This sets the phase of the direct-path peak to zero, while the basal echo peak becomes: $e^{j(\phi_m + \phi_b)} e^{-j(\phi_m + \phi_d)} = e^{j(\phi_b - \phi_d)}$. This procedure removes the random phase ϕ_m , causing all chirps to be in-phase and enabling coherent summation. Provided that

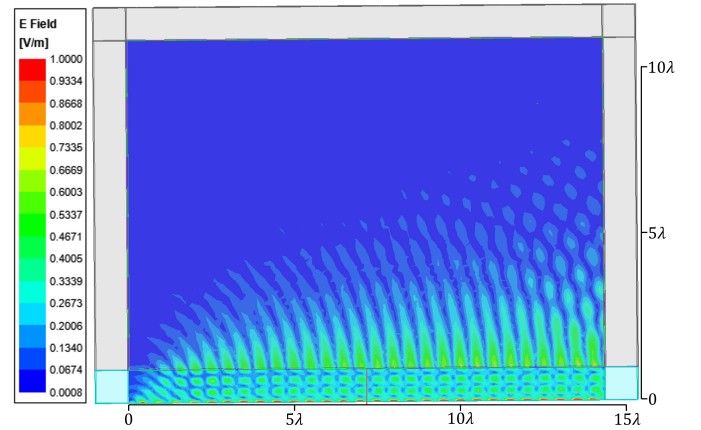


Fig. 6. HFSS simulation demonstrating that the evanescent waves extend roughly 6λ above the surface and can be captured by antennas close to the ice surface. The simulation space is made large compared to wavelength ($15\lambda \times 11\lambda$) to ensure that the finite width of the incident plane wave (moving from bottom left to top right) does not impact the antenna (far right). The left half of the simulation space is ignored because the finite wave port makes that side of the solution a poor approximation for an infinite plane wave.

the direct path is detectable, this synchronization technique enables basal echo recovery from below the noise floor at any antenna offset, provided that noise is additive rather than multiplicative.

Ranging can be estimated using the direct path and the antenna separation. The transmit time (t_0) can be estimated from the time the direct path was received (t_d) and the antenna separation (x)

$$t_0 = t_d - \frac{x}{c}. \quad (3)$$

The ice thickness at the midpoint between the antennas can be estimated using the transmit time, echo receive time (t_b), and the ice relative permittivity (ϵ_r)

$$h = \sqrt{\left(\frac{c(t_b - t_0)}{2\sqrt{\epsilon_r}}\right)^2 - \frac{x^2}{4}}. \quad (4)$$

IV. RESULTS

A. Total Internal Reflection

TIR has been suggested to limit bistatic antenna separation on ice [27]; however, we find in HFSS that this is not a limiting factor for ground-based systems since the surface is within the antenna's near field. The antenna's receive power is shown in Fig. 7 for two different heights above the ice. TIR is captured by the simulation, as shown in Fig. 6; consequently, the antenna simulated at 8λ from the ice surface receives very little power at large bistatic angles. However, the evanescent waves extend about 6λ above the surface (Fig. 6) and are captured by the antenna $\lambda/10$ above the ice. As a result, the ground-based antenna experienced little loss at increasing bistatic angle, with a receive power remaining around -26 dB (Fig. 7).

B. Static Long-Offset Demonstration in Antarctica

In December 2018, we tested the synchronization method and hardware at Whillans Ice Stream, West Antarctica, using offsets longer than those possible with traditional

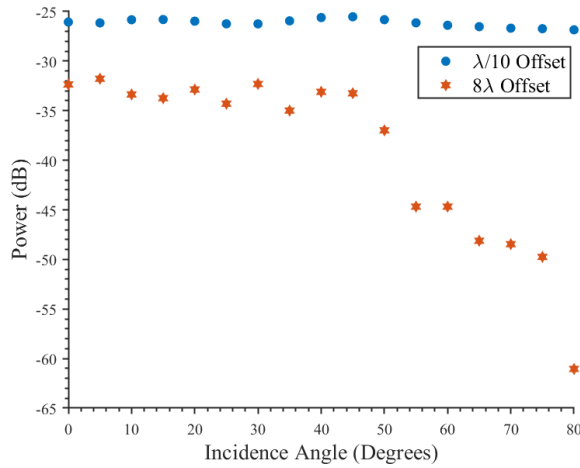


Fig. 7. Receive power from a plane wave traveling from ice to air for various incidence angles and two different antenna heights above the ice— 8λ and $\lambda/10$. Little power is received past the critical angle when the antenna is far from the ice surface, indicating that TIR occurs. However, TIR does not significantly impact an antenna near the ice surface.

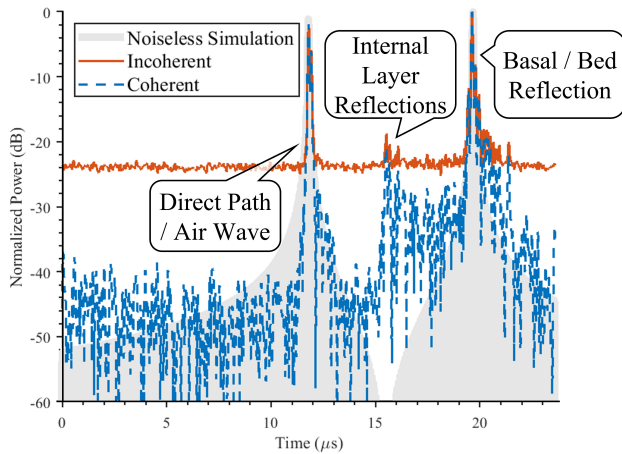


Fig. 8. Coherently averaging 123 matched filtered, upsampled chirps enabled bed detection at an antenna separation of 1300 m in 797-m-thick ice with 44-dB SNR at Whillans Ice Stream, Antarctica. Coherent summation performs better than incoherent summation, making both the bed echo and internal layers clearly visible. Furthermore, the noise floor approached the interference level of the noiseless simulation.

GPRs [24], [26], [27]. The transmitter and receiver were held stationary at the separations of 300, 600, 900, and 1300 m. Using an ApRES with antenna separation <10 m (see Appendix C), we measured the ice column at the bistatic transmitter to be 797 m thick without firn correction using a permittivity of 3.18. Even with our modest 100-mW transmit power, the processing chain successfully recovers the bed reflection at all antenna separations to SNRs greater than 44 dB as well as the internal layers in measurements at offsets of 600–1300 m [39]. The internal layers for the 300-m antenna separation are inseparable from the direct path. The 1300-m antenna separation result is shown in Fig. 8 and shows that the noise floor approaches the interference level of a noiseless simulation. Without upsampling nor parabolic fitting, the estimated ice thicknesses at increasing bistatic antenna separation are 787, 786, 777, and 784 ± 29 m that match the PRES measured ice thickness of 797 m at 10-m antenna separation.

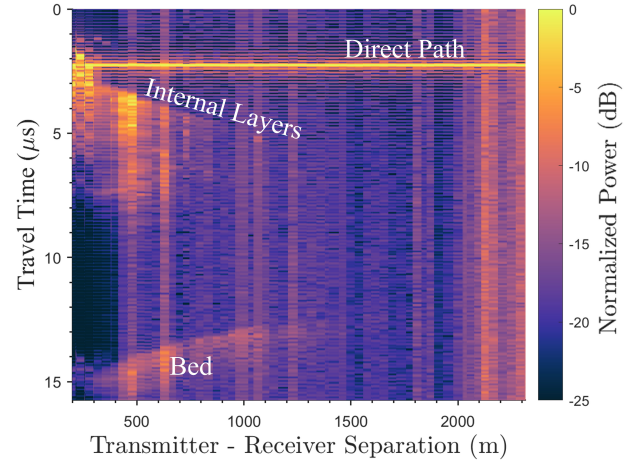


Fig. 9. Bistatic quasi-radargram of Store Glacier, Greenland, formed by towing the receiver away from the transmitter. Chirps are aligned in time based on the direct path that is the bright yellow line around $2 \mu\text{s}$. Note that $0 \mu\text{s}$ is arbitrarily defined as $2.6 \mu\text{s}$ before the direct-path arrival. The bright patch between 4 and $8 \mu\text{s}$ is the return from internal layers, which slopes away from the direct path at longer offsets due to the bistatic geometry. The bed echo appears at 14–16 μs and also curves due to the bistatic geometry.

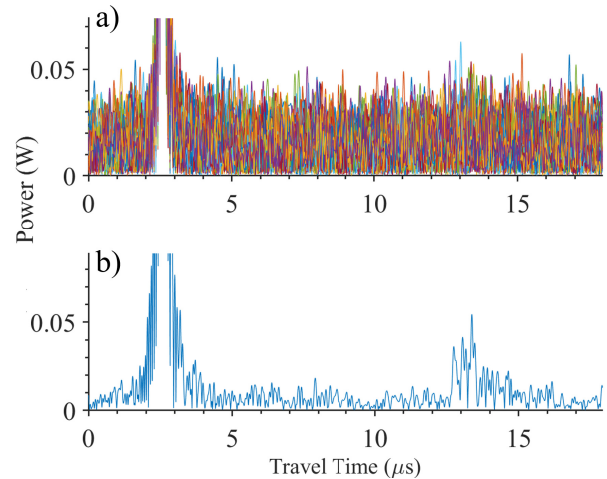


Fig. 10. (a) At 1450-m antenna separation and 1028-m ice thickness, we collected 46 chirps (each plotted a different color) where the direct path is detectable and the bed reflection is buried by noise. The direct path is 13 dB above the noise floor, but we clip the y-axis to focus on noise reduction provided by coherent summation. (b) To recover the basal echo from the noise, we phase-aligned and coherently summed the 46 chirps to produce the blue line, which expresses the basal echo around $13 \mu\text{s}$.

C. Moving Long-Offset Demonstration in Greenland

In the summer of 2019, we tested the system on a moving platform at Store Glacier, Greenland, where the ice was measured to be 1028 m thick (see Appendix C). The receiver traveled 199–2316 m away from the static transmitter collecting the traces plotted in Fig. 9 [39]. Few chirps are summed per Fresnel zone due to the speed of the receiver, except when we recorded statically at 198-, 1051-, 1450-, and 2027-m antenna separations. At these locations, the SNR is higher from summing more chirps. The 1450-m antenna separation is the last high SNR location where we collect sufficient chirps for bed echo recovery, which is shown in Fig. 10. At this offset, the noise floor is too high to detect the basal echo in any single trace; however, coherent summation reveals the basal echo.

The basal echoes with SNR better than 12 dB and misalignment less than $2 \mu\text{s}$, values that were empirically found to yield the best results, are used to estimate the basal echo power and ice thickness along the transect. The resulting data are plotted in Fig. 11. Correcting received power by geometric spreading and neglecting the angular dependence of the antenna pattern and reflection coefficient yield an approximate one-way average power attenuation of 43.3 dB/km. Following [13], [26], the one-way average attenuation is estimated as the slope of power versus path length.

D. Evaluating Coherence

To assess the performance of our synchronization approach, we compared the SNR gain of data and theory. As discussed in Appendix B-A, coherently summing N chirps theoretically results in an SNR gain of N , while incoherently summing only provides \sqrt{N} SNR gain. The SNR is defined as the ratio of the average signal power to the standard deviation of the noise power (see Section B-A)

$$\text{SNR} = \frac{\text{Average Signal Power}}{\text{Standard Deviation of Noise Power}} \quad (5)$$

$$= \frac{E[|v(t)|^2]}{\bar{\sigma}_{\text{noise PW}}}. \quad (6)$$

Here, $E[\]$ denotes the expectation value, $v(t)$ is the signal voltage, and $\bar{\sigma}_{\text{noise PW}}$ is the standard deviation of the noise power. The noisy 1300-m Antarctica data show an SNR growth of N for coherent summation as shown in (Fig. 12), demonstrating that the processing technique is effectively synchronizing chirps.

V. DISCUSSION

A. Greenland Data

In our Greenland data, the basal echo slowly fades below the noise floor because too few chirps are collected per Fresnel zone to recover the basal echo. Most data points in Fig. 11 could only sum eight chirps, meaning that the high noise was only dampened by a factor of 8 leading to high variability of received power. This uncertainty further worsens with increasing offset and decreasing SNR. A more accurate attenuation rate could be recovered by accounting for measurement uncertainty in the least-squares fit and reducing uncertainty with a modified experiment design. A more accurate inversion can be obtained at the cost of resolution by summing more chirps at each antenna separation and reducing the number of station locations. Therefore, we recommend performing static measurements and increasing the number of chirps summed with distance to ensure high SNR rather than taking measurements on a moving platform. Obtaining sufficiently high SNR though summing large numbers of chirps is a day-long process. Therefore, we recommend that future operations deploy 2–3 receivers at different offsets in the morning, conduct alternate experiments during the day, and retrieve the receiving units in the evening. Enabling all-day recording will require a larger battery and flash drive with more capacity. Furthermore, future attenuation estimations should account for the angular dependence of antenna separation and reflection coefficient.

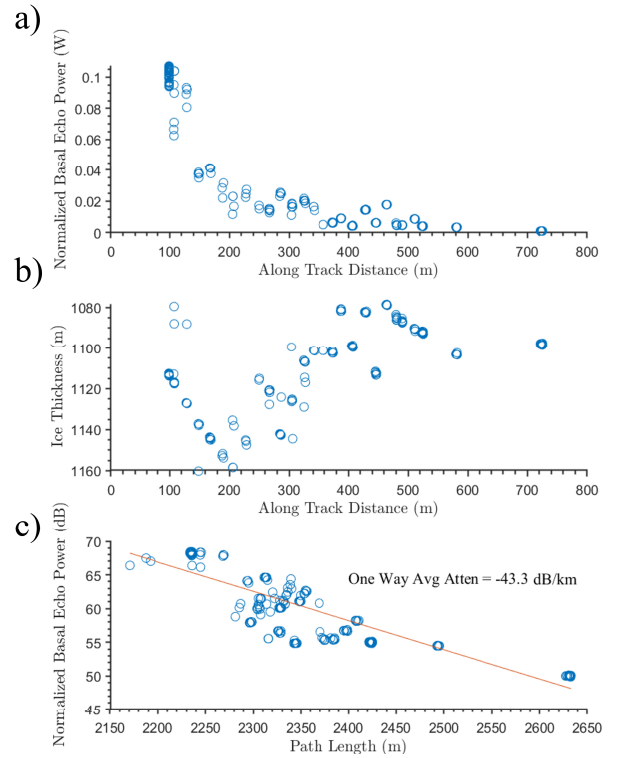


Fig. 11. Normalized basal echo power and ice thickness were extracted from the Greenland data, showing that Store Glacier has a one-way average power attenuation of -43.3 dB/km at 330 MHz. (a) Scaled basal echo power decays exponentially as a function of along-track distance to the reflection point. The basal echo occurs at roughly half the antenna separation, so the x -axis is half the transmitter–receiver separation. (b) Ice thickness was estimated using (4) after subsample estimation travel time using parabolic fitting to the direct and basal peaks. Ice depth is estimated at the specular reflection point, so the x -axis is half the transmitter–receiver offset. (c) Basal echo power was scaled to account for geometric spreading and then plotted against path length such that the slope of the best fit line is the one-way attenuation.

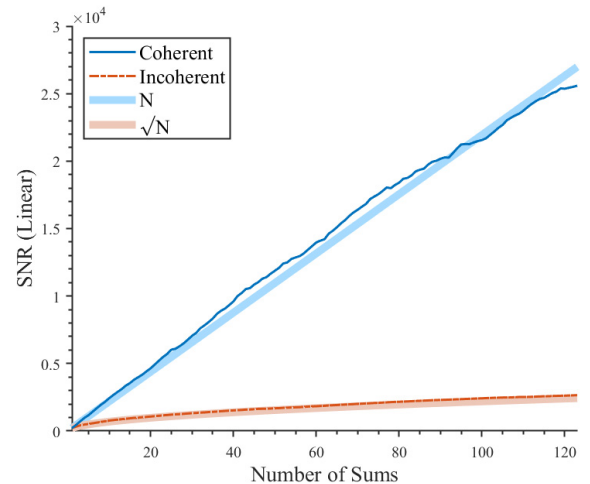


Fig. 12. Comparison of the SNR ($\mu_{\text{signal PW}}/\bar{\sigma}_{\text{noise PW}}$) for coherent and incoherent summation of 1300-m offset sounding data at Whillans Ice Stream. The SNR increases as \sqrt{N} for incoherent summation and N for coherent summation. Coherent summation improves the SNR from 23.4 to 44 dB over 123 sums.

B. Total Internal Reflection

Counter to suggestions in [27], our results demonstrate that ground-based bistatic systems are not limited by TIR.

TIR is derived from ray theory and can only be applied in an antenna's far-field, meaning that it is not applicable for the ice-air interface of ground-based measurements [40]. Based on the results in Fig. 7, we conclude that ground-based surveys do not suffer from TIR, but note that airborne systems flying above 6λ will experience TIR and consequentially be unable to use angles beyond the critical angle. We confirm our simulated result of antenna coupling for ground-based systems by detecting the basal echo beyond the critical angle in field experiments. For isotropic ice with a relative permittivity of 3.18, the critical angle is 34° off-nadir, which corresponds to a bistatic offset of 1392 m at Store Glacier and 1079 m at Whillans Ice Stream. We exceeded these distances with maximum antenna separations of 1450 and 1300 m.

C. Surface Conditions and Safety

The requirement that bistatic radar experiments can be ground-based to capture the evanescent waves causes an experimental design to be influenced by glacial surface features. Radars aboard autonomous rovers or "leap-frogging" quadcopters can survey most glacial terrains, but manned bistatic surveys are limited to areas that people can safely cross. Safety is paramount in field research, so some areas, such as crevasse fields, cannot be monitored with manned bistatic surveys. However, in our team's experience on high-strain glaciers at Thwaites Eastern Shear Margin and Store Glacier, crevasse fields were sparse and avoided with pre-season scouting and planning. While crevasse fields only hamper bistatic surveys due to the human component, some nonhazardous features innately impede radar measurements. Specifically, high concentrations of moderately saline water cause high attenuation rates and require an impractically large number of coherent sums to recover the basal echo. For example, buried supraglacial lakes, water-saturated surface snow, and exceptionally saline firn aquifers can obstruct the basal echo. Most firn aquifers will not be briny enough to cause this problem [41] and can be imaged with our technique.

Most nonhazardous surface features do not adversely impact bistatic radar data. The Store Glacier data shown in Fig. 9 were collected across ablation zone hummocks, small supraglacial streams, and healed crevasses with no noticeable degradation to the data. The primary impact of the ablation zone hummocks, as shown in Fig. 13, was that experiments had to be conducted on foot rather than snowmobile. The direct path is seen at all offsets even though the transect crested a small hill such that the transmitter was no longer in line-of-sight at the end of the transect. Most surface features do not impact the radar data because the electromagnetic wave passes through and over features with minimal attenuation.

D. Extending Maximum Antenna Separation

Since TIR is not a limiting factor, the basal reflection can be recovered with our synchronization approach at any antenna separations given sufficient record time, a detectable direct-path signal, and additive rather than multiplicative noise. For example, at 10000-m separation, geometric spreading losses would result in a 79-dB weaker signal than the direct-path signal we detect at 1450 m over 1028 m of ice at Store Glacier,



Fig. 13. Eliza Dawson carries the receiver across small supraglacial streams and hummocks to the next measurement at Store Glacier, Greenland. These surface features do not degrade the radar data.

Greenland. While this would make the signal undetectable for our current experiment configuration because the direct path is only 13 dB above the noise floor for that measurement, there are many adjustments that could be made to the experiment to boost the direct-path SNR. The transmitter only sends 100-mW chirps, which could be increased to 10 W with amplifiers. Better pulse compression gain could be obtained by extending the chirp length from 77 ms to 1 s. With the antennas pointed at nadir, the antenna pattern along the direct path has a gain of 0 dB, but different antennas with 9-dB gain could be used and pointed along the direct path. Together, these changes would improve the SNR by 112 dB, overcoming the 79-dB additional loss at 10000 m and enable detection of the direct path. Reorienting the antenna degrades the bed echo power and longer offsets accumulate more attenuation, but these echo losses can be overcome by the N SNR gain of coherent summation that we demonstrate in Fig. 12. Such a measurement is very time-consuming due to the slow write speeds of the E312, but if a continuous recording SDR such as an x310 is used and chirps are sent without break, the measurement could be completed in a few tens of seconds. These recommendations are a few methods to extend the maximum antenna separation achievable with this system.

E. Future Work

The processing-based time and phase synchronization approach presented here enable cable-less bistatic radar measurements without the hardware complexity introduced by active synchronization. The direct-path synchronization approach could be applied to distributed orbital radar sounders, such as [42] and [43], for wireless beamforming without adding hardware and introducing a point of failure. This technology could also be used to estimate basal material properties below a glacier. As shown in Fig. 2, the radar reflection coefficient is dependent on bistatic angle, antenna polarization, and basal material. Collecting data with many antenna separations and both polarizations would enable inversions of basal material, revealing if the bed is frozen or thawed and bedrock or till [11], [36].

With antenna separations larger than ice thickness possible, radar glacial tomography becomes feasible. Producing a

high-fidelity map of ice temperature, ice crystal fabric, and water content would not only capture the current state of the glacier but also provide clues for how it may evolve in the future. For example, mapping temperate zones created by the transition from slow to fast flow could shed light on the hypothesis that thermal pockets localize and stabilize shear margin location [22], [23]. Measuring the thermal regime at the ice–bed interface could decipher whether the basal thermal regime is frozen or thawed to characterize the rate of sliding [44]. As the bed is thawed and the ice above is warm, liquid water can exist, which acts as lubrication to facilitate faster sliding [45], [46] and can feed into subglacial hydrological networks [47]. Measuring the thermal structure could also provide constraints on geothermal heat flux, which is an important parameter for ice-sheet models [48]–[50]. Evaluating the ice fabric reveals a preferred deformation direction caused by ice crystal orientation [5]. Mapping the spatial distribution of subsurface aquifers in ice could provide information to close the water budget [9], [41]. Our work to enable large antenna separations makes highly constrained inversions possible to estimate glacial properties with the fidelity required for glaciological interpretation.

VI. CONCLUSION

We demonstrated a processing-based synchronization approach that enables cable-less bistatic radar experiments without the hardware complexity introduced by wireless active synchronization methods. In validation testing (data available at [39]), our processing method recovered a 100-mW transmit signal reflecting from the bed of a 1028-m-thick glacier with an antenna separation of 1450 m at Store Glacier, Greenland. We achieve a factor of N SNR gain by coherently summing N chirps, which enables signal recovery at any antenna separation provided unlimited time, a detectable direct path, and additive rather than multiplicative noise. As demonstrated in HFSS simulation and experiments beyond the critical angle, TIR does not limit the maximum attainable antenna separation for ground-based measurements. The key to our synchronization procedure is phase alignment by multiplying the entire chirp by the complex conjugate of the phase of the matched filtered direct path. Subsample time alignment is achieved with parabolic peak estimation and time shifting in the frequency domain. The resulting code, available on GitHub at [38], transforms a simple SDR receiver paired with any LFMCW transmitter into a coherent bistatic radar capable of recovering echoes at large bistatic antenna separation. Our system opens the doors to full tomographic inversions of temperature, ice fabric, and basal material at the spatial and thermal scales that influence ice-sheet flow and stability.

APPENDIX A PRACTICAL CONSIDERATIONS

A. Antenna Orientation

Antenna orientation can be safely neglected in monostatic radar sounding but can have a significant impact on SNR in bistatic experiments. The reflected power for the two antenna orientations diverges beyond 10° off-nadir that is exceeded

in bistatic experiments. The angle-dependent reflection coefficients for s-pol (electric field parallel to the surface and perpendicular to transect) and p-pol (magnetic field parallel to the surface and parallel to transect) are given in (7) and (8) [51], [52]. In the following, $\Gamma_{E\parallel}$ denotes the reflection coefficient for s-pol where the electric field is parallel to the surface, $\Gamma_{H\parallel}$ is the reflection coefficient for p-pol where the magnetic field is parallel to the surface, and η is the wave impedance in each medium where 1 denotes the material from which the wave originates and 2 indicates the material a wave impinges on. These equations do not make loss assumptions. Note that other literature (e.g., [53], [54]) wraps the imaginary part of permittivity ϵ'' into an “effective” conductivity: $\sigma = \sigma_s + \omega\epsilon''$

$$\Gamma_{E\parallel} = \frac{\eta_2 \cos(\theta_t) - \eta_1 \cos(\theta_i)}{\eta_2 \cos(\theta_t) + \eta_1 \cos(\theta_i)} \quad (7)$$

$$\Gamma_{H\parallel} = \frac{\eta_2 \cos(\theta_t) - \eta_1 \cos(\theta_i)}{\eta_2 \cos(\theta_t) + \eta_1 \cos(\theta_i)} \quad (8)$$

$$\eta = \sqrt{\frac{\mu}{\epsilon'}} (1 - j \tan \delta)^{-1/2} \quad (9)$$

$$\cos(\theta_t) = \sqrt{1 - \frac{\mu_1 \epsilon'_1 (j \tan \delta_1 - 1)}{\mu_2 \epsilon'_2 (j \tan \delta_2 - 1)} \sin^2(\theta_i)} \quad (10)$$

$$\tan \delta = \frac{\sigma_s + \omega \epsilon''}{\omega \epsilon'} \quad (11)$$

Here, θ_i is the incident angle to the surface normal, θ_t is the transmission angle to the surface normal, $\tan \delta$ is the loss tangent, ω is the frequency in radians per second, ϵ' is the real part of permittivity, ϵ'' is the imaginary part of permittivity, and μ is the permeability. P-polarization orientation can reflect zero power back to the surface at the Brewster angle, which occurs for low loss materials such as in Fig. 2(a)–(c) and (f). The more conductive basal materials shown in Fig. 2(d) and (e) reflect significantly less power around 60° and 70° but do not hit zero reflected power. The curves are characteristic of basal material, meaning that bistatic experiments could match data to the angular-dependent reflectivity curves to estimate the basal material. This experiment is strictly intended to demonstrate the technology that enables large offsets, so we use s-polarization since it reflects more power than p-polarization at large angles. Our demonstration extends to p-polarization but would require longer experiment time to obtain sufficient coherent sums for high SNR.

B. Bandwidth

1) *Bandwidth Impact on Single Reflection*: Ignoring interference from the direct path, bandwidth should have no impact on SNR after matched filtering, which we investigate empirically. We measure chirps of different bandwidths with the same chirp length (τ) directly from the ApRES, matched filter the chirps, and calculate SNR as: $((pk^2 - E[n(t)^2]) / (E[n(t)^2]))$ (Fig. 14). We find that the measured SNR remains roughly constant across bandwidth. Increasing bandwidth increases the amount of thermal noise ($kT_{\text{sys}}B$), which counteracts the improving pulse compression gain (τB) in the matched filter, where τ is the chirp length.

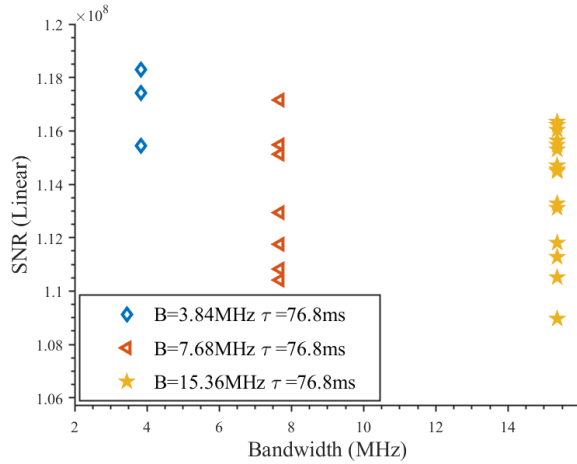


Fig. 14. Multiple chirps were received for a given bandwidth and the SNR of each individual chirp was plotted. Bandwidth does not significantly correlate with the SNR output of the matched filter. The matched filter's pulse compression gain of τB cancels the thermal noise's proportionality to B . When the chirp length (τ) is held constant, then the SNR of the matched filter output does not change with bandwidth.

Consequently, the bandwidth does not impact the SNR of a single chirp.

Matched filtering is used to maximize the SNR before summation. Range compressing an LFM CW $v(t)$ with itself leads to a signal with an absolute value given by (see [56, Appendix 3A.1])

$$\int_{-\infty}^{\infty} |v(t)|^2 dt (\tau - |t|) \text{sinc} \left[\frac{Bt}{\tau} (\tau - |t|) \right], \quad |t| \leq \tau \quad (12)$$

where B is the bandwidth and τ is the chirp length. This is a triangle function multiplied by a sinc function with a peak amplitude of the integral of the signal squared. The width of the triangle is two times the chirp length and the half-power width of the sinc is $(1/B)$. The width of the matched filtered chirp is controlled by the bandwidth and B does not impact the signal peak after matched filtering. It is further explained in Appendix B-C how matched filtering cancels the bandwidth dependence of noise power to cause SNR to be independent of bandwidth.

2) *Interference From Direct Path*: Although bandwidth does not influence the SNR of a single matched filtered chirp, it does impact the interference from nearby chirps. In Fig. 15, the matched filter response of the simulated direct path (blue) overlaps with the bed reflection (red) and causes interference. The sinc function decays faster and causes less interference for higher bandwidth.

In practice, the interference from the direct path appears as coherent noise, which places a limit on the maximum achievable SNR for coherent summation. Fig. 8 shows the real data collected from Whillans Ice Stream, West Antarctica, at the 1300-m separation between the transmitter and receiver antennas approaching the interference simulated for noiseless chirps. In data from this experiment, the interference decreases as antenna separation increases due to the rapid $(1/d^2)$ decay of the direct path at small separations. Since there is more interference at smaller separations, future measurements may use higher bandwidth at small antenna separations and

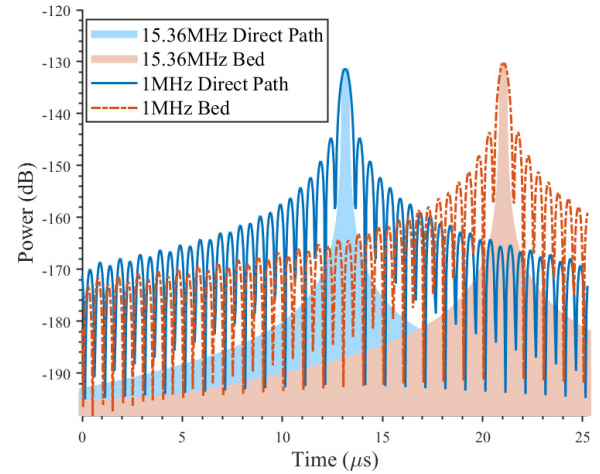


Fig. 15. Noiseless chirps are simulated for a 1300-m antenna separation with different bandwidths while holding all other parameters constant. The direct path (blue line) interferes less with the bed reflection (red line) for higher bandwidths.

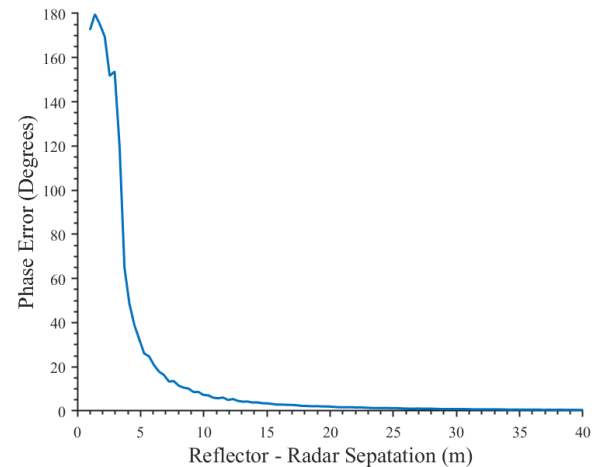


Fig. 16. Phase shift introduced by multipath is plotted as a function of distance between a reflector and the radar transmitter or receiver (whichever is closer). The signal of interest has a phase of $\theta_b - \theta_d$ after phase alignment; however, there is an additional phase shift caused by interference from signals reflected from nearby objects such as snowmobiles. The phase shift to both the bed reflection and the direct path is computed with and without a $3 \text{ m} \times 1 \text{ m}$ PEC reflector, and then, the phase error is calculated.

lower bandwidth for large antenna separations. Direct-path suppression may also be investigated.

C. Nearby Reflectors

Our phase alignment method relies on a constant phase shift between the direct path and bed reflection for stacking traces, but reflections from nearby objects can introduce phase noise and degrade the SNR gain of coherent stacking. Reflections from nearby moving metal objects such as snowmobiles are of particular concern. A conductor can produce similar amplitude waves to the signal of interest if the reflector is near the radar. If the reflector moves between stacking, then the summed traces are not phase-aligned and can destructively interfere. Alternatively, if reflectors are in a constant position with respect to the survey geometry, such as the snowmobile towing the receiver, there will be a constant phase bias, which does not impact the coherent summation. When the metal object is

far from both the transmitter or receiver, then the power decays as $(1/(d/2)^4)$, which is greater than the geometric spreading loss from the direct path and bed reflection. Therefore, the magnitude of unwanted multipath signal is low enough that the interference is minimal.

We conducted MATLAB simulations to estimate the separation distance that a snowmobile could drive parallel to the bistatic transect and cause less than 10° of phase error. The snowmobile is approximated as a $3 \text{ m} \times 1 \text{ m}$ perfect electric conductor plane and we used an ice thickness of 1000 m. This simulation computes the phase shift caused by a reflector to both the direct path and bed reflection and then finds the phase error associated with the bed reflection after phase alignment with and without the snowmobile reflector (Fig. 16). Note that the far field for our antenna is 2.2 m and the far field for the metal reflector is 22 m, but near field effects and coupling are not considered. The far-field influence to the phase error drops below 10° by 9-m transect separation and 1° by 28 m.

APPENDIX B

SNR OF COHERENT AND INCOHERENT PROCESSING

A. SNR Definition

SNR is typically defined as a ratio of average power for applications such as link budgets, while in imaging applications, SNR can be described as the ratio of the signal and standard deviation of the noise. To quantify signal detectability, we use the standard deviation definition, which quantifies how much a signal peak protrudes from surrounding noise fluctuations [56]–[58]. For example, an increasing number of incoherent sums make it easier to detect a signal since the noise standard deviation decreases, but this is not reflected in the average power ratio that remains constant. While the SNR definitions are not equivalent for incoherent summations, they are interchangeable for coherent summations. Here, SNR is defined as

$$\text{SNR} = \frac{E[|s(t)|^2]}{\bar{\sigma}_{\text{noise PW}}} \quad (13)$$

where $s(t)$ is the signal voltage. When coherently summing zero-mean white Gaussian noise, the standard deviation of the noise power is equivalent to the variance of the noise voltage $[n(t)]$ (see B-D) scaled by τR to preserve units. Expanding the definition of variance and using the fact that noise voltage is zero mean, we find that $\bar{\sigma}_{\text{noise PW}}$ is equivalent to the average noise power

$$\begin{aligned} \text{If: } \bar{\sigma}_{\text{noise PW}} &= \frac{1}{\tau R} \text{var}(n(t)) \\ \text{Then: } &= \frac{1}{\tau R} \text{var}(n(t)) + \frac{1}{\tau R} |E[n(t)]|^2 \\ &= E \left[\frac{|n(t)|^2}{\tau R} \right] = \bar{\mu}_{\text{noise PW}}. \end{aligned} \quad (14)$$

This allows the SNR definition from (13) to be simplified to a ratio of average powers

$$\begin{aligned} \text{SNR} &= \frac{E[|s(t)|^2]}{E[|n(t)|^2]} \\ \text{if } E[n(t)] &= 0, \quad \text{var}(n(t)) = \sqrt{\text{var}(|n(t)|^2)}. \end{aligned} \quad (15)$$

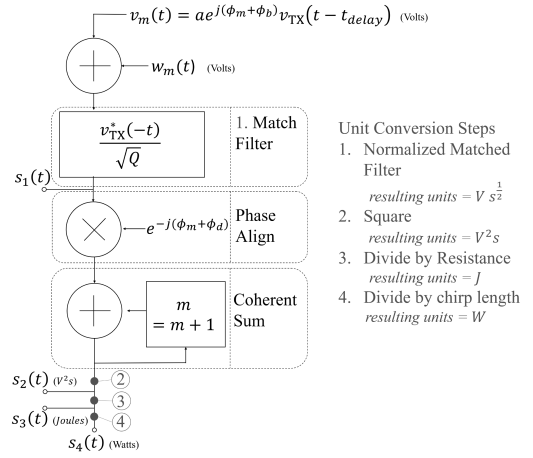


Fig. 17. Representation of the transforms a signal undergoes while passing through the processing chain.

This simplification holds for zero-mean white Gaussian noise and consequentially does not apply to incoherent summation.

B. Note About Units

Proper unit conversions allow comparison of the processed output power with the radar power equation and is an integral part of our processing chain [59]. A summary of the steps in the processing chain is given in the following, shown in Fig. 17, where we highlight the unit conversions.

- 1) Perform normalized matched filter by convolving with $((v_{TX}^*(-t))/\sqrt{Q})$ (resulting units = $V s^{1/2}$), where

$$Q (V^2 s) = \int_{-\infty}^{\infty} |v(t) (\text{Volts})|^2 dt \quad (16)$$

then coherently average by complex summing N chirps and dividing by N (resulting units = $V s^{1/2}$).

- 2) Square (resulting units = $V^2 s$).
- 3) Divide by resistance to change to units of energy (resulting units = joules).
- 4) Convert to power by dividing by chirp length (τ) (resulting units = W).

C. Power in Coherently Processed Signal

Our processing chain is shown in Fig. 17, where m denotes the chirp number, ϕ_m is the unknown phase difference between the transmitter and receiver LOS, ϕ_b is the phase shift accumulated by the wave which reflected off the bed, ϕ_d is the phase shift accumulated from propagating directly between the transmitter and receiver through the air, $v_m(t)$ is the receive bed echo, a is a scalar accounting for attenuation loss, v_{TX} is the transmit chirp, t_{delay} is the time between transmit and receive, and $w_m(t)$ is the Gaussian white noise.

The signal passes through a unity gain matched filter, which is represented as convolution with $((v_{TX}^*(-t))/\sqrt{Q})$, where

$$Q = \int_{-\infty}^{\infty} |v_{TX}(t)|^2 dt. \quad (17)$$

Following the matched filter step, the signal at $t = t_{\text{delay}}$ is:

$$\begin{aligned} s_1(t_{\text{delay}}) &= \int_{-\infty}^{\infty} v_m(\tau) \frac{v_{\text{TX}}^*(\tau - t)}{\sqrt{Q}} d\tau \Big|_{t=t_{\text{delay}}} \\ &= \frac{ae^{j(\phi_m + \phi_b)}}{\sqrt{Q}} \int_{-\infty}^{\infty} v_{\text{TX}}(\tau - t_{\text{delay}}) v_{\text{TX}}^*(\tau - t_{\text{delay}}) d\tau \\ &= ae^{j(\phi_m + \phi_b)} \sqrt{Q} \quad (\text{V s}^{1/2}). \end{aligned} \quad (18)$$

After phase alignment, coherent summation, and magnitude square, the basal echo becomes

$$\begin{aligned} s_2(t_{\text{delay}}) &= \left| \sum_{m=1}^N ae^{j(\phi_m + \phi_b)} e^{-j(\phi_m + \phi_d)} \sqrt{Q} \right|^2 \\ &= |aN\sqrt{Q}e^{j(\phi_b - \phi_d)}|^2 \\ &= a^2N^2Q \quad (\text{V}^2\text{s}). \end{aligned} \quad (19)$$

After dividing by resistance (R), the signal is the average energy in the basal echo amplified by N^2

$$\begin{aligned} s_3(t_{\text{delay}}) &= a^2N^2 \frac{1}{R} \int_{-\infty}^{\infty} |v_{\text{TX}}(t)|^2 dt \\ &= a^2N^2 E_{\text{TX}} \quad (\text{Joules}) \end{aligned} \quad (20)$$

$$\text{Where Energy} = \int_{-\infty}^{\infty} \frac{|v(t)|^2}{R} dt. \quad (21)$$

Step 4 in Fig. 17 converts this energy into power by dividing by the chirp length (τ). Recognizing that the power in the echo (P_{echo}) is the transmit power (P_{TX}) attenuated by a^2 , the output of the processing chain is the power in the basal echo amplified by the number of sums squared

$$s_4(t_{\text{delay}}) = \frac{a^2N^2E_{\text{TX}}}{\tau} = a^2N^2P_{\text{TX}} = N^2P_{\text{echo}} \quad (\text{Watts}). \quad (22)$$

D. Coherent Summation Noise Statistics

The impact of coherent summation on the statistics of white Gaussian noise is summarized to aid evaluation of $\tilde{\sigma}_{\text{noise PW}}$, the denominator for SNR [see (13)]. Since the matched filter is linear time invariant, the white noise passing through it remains normally distributed. The white noise random variable following matched filtering is given by W ($\text{Vs}^{1/2}$) composed of the real X and imaginary Y random variables that are normally distributed around zero [$Y \sim X \sim N(0, \tilde{\sigma}_v^2)$]

$$\begin{aligned} \text{Coherent Noise} &= \sum_{m=1}^N W_m \\ &= \sum_{m=1}^N X_m + j \sum_{m=1}^N Y_m \\ &= Z + jQ \\ Z &\sim Q \sim N(0, N\tilde{\sigma}_v^2). \end{aligned} \quad (23)$$

Converting from units of $\text{Vs}^{1/2}$ to power, we complete unit conversion steps 2–4 by taking the square of the absolute value, divide by resistance (R), and divide by chirp length (τ). Squaring folds the Gaussian distributions across the y -axis to form a Rayleigh distribution. This is also a chi distribution with two degrees of freedom, but stretched by the Gaussian

TABLE I
COMPARISON OF NOISE POWER STATISTICS
AFTER N COHERENT OR INCOHERENT SUMS

	Coherent $\text{Vs}^{1/2}$	Coherent PW	Incoherent PW
Expression	$\sum_{m=1}^N W_m$	$\frac{1}{\tau R} \left \sum_{m=1}^N W_m \right ^2$	$\sum_{m=1}^N \frac{ W_m ^2}{\tau R}$
Distribution	$N(0, N\tilde{\sigma}_v^2)$	χ_2^2	χ_{2N}^2
Mean	0	$2N\tilde{\sigma}_v^2 \frac{1}{\tau R}$	$2N\tilde{\sigma}_v^2 \frac{1}{\tau R}$
St. Deviation	$\sqrt{2N}\tilde{\sigma}_v$	$2N\tilde{\sigma}_v^2 \frac{1}{\tau R}$	$2\sqrt{N}\tilde{\sigma}_v^2 \frac{1}{\tau R}$
Variance	$2N\tilde{\sigma}_v^2$	$4N^2\tilde{\sigma}_v^4 \frac{1}{\tau^2 R^2}$	$4N\tilde{\sigma}_v^4 \frac{1}{\tau^2 R^2}$

voltage variance ($N\tilde{\sigma}_v^2$), resistance, and chirp length. The scaling factor is multiplied by the mean ($k = 2$) and standard deviation ($\sqrt{2k} = 2$). Therefore, the coherent noise power has a mean of $kN\tilde{\sigma}_v^2(1/\tau R) = 2N\tilde{\sigma}_v^2(1/\tau R)$ and standard deviation of $\sqrt{2k}N\tilde{\sigma}_v^2(1/\tau R) = 2N\tilde{\sigma}_v^2(1/\tau R)$

$$\begin{aligned} \text{Coherent Noise Power} &= \frac{1}{R} \left| \sum_{m=1}^N W_m \right|^2 \\ &= \frac{1}{R} [Z^2 + Q^2] \\ &\sim \chi_2^2, \quad \mu = \frac{2N\tilde{\sigma}_v^2}{\tau R} \quad \tilde{\sigma}^2 = \frac{4N^2\tilde{\sigma}_v^4}{\tau^2 R^2}. \end{aligned} \quad (24)$$

E. SNR of Coherently Processed Output

Coherent processing maintains the conditions of having zero-mean voltage and $\tilde{\sigma}_{\text{noise PW}} = (1/R)\text{var}(n(t))$ (highlighted in Table I), allowing the SNR definition [see (13)] to be reduced to a ratio of average powers [see (15)]. The power in our signal of interest is N^2P_{echo} as shown in Appendix B-C. The average noise power after passing through the processing chain is

$$\begin{aligned} &\frac{1}{R\tau} E \left[\sum_n w_n(t) * \frac{v_{\text{TX}}^*(-t)}{\sqrt{Q}} \sum_m w_m^*(t) * \frac{v_{\text{TX}}(-t)}{\sqrt{Q}} \right] \\ &= \frac{1}{R\tau} \sum_{m=1}^N E [w_m(t) v_{\text{TX}}^*(-t) w_m^*(t) * v_{\text{TX}}(-t)] \frac{1}{Q} \\ &\quad + \frac{1}{R\tau} E \left[\sum_{n \neq m} w_n(t) * v_{\text{TX}}^*(-t) \sum_{m \neq n} w_m^*(t) * v_{\text{TX}}(-t) \right] \frac{1}{Q} \\ &= \frac{1}{R\tau} \sum_{m=1}^N E \left[\left| w_m(t) * \frac{v_{\text{TX}}^*(-t)}{\sqrt{Q}} \right|^2 \right] \\ &= \frac{1}{\tau} \int_{-\infty}^{\infty} \frac{|W_m(f)|^2 |V_{\text{TX}}(f)|^2}{R\tau Q} df \\ &= NkT \frac{1}{\tau} \frac{\int_{-\infty}^{\infty} |V_{\text{TX}}(f)|^2 df}{Q} = \frac{NkT}{\tau}. \end{aligned} \quad (25)$$

The denominator is evaluated by splitting it into $m \neq n$ and $m = n$ parts. The sums over m and n are independent when $m \neq n$ enabling the expectation value to be split to the multiplying terms. The noise signal remains a zero-mean Gaussian after coherent voltage processing, so the expectation value when $m \neq n$ is 0. After removing the $m \neq n$ term, the equation is converted from convolution to

multiplication by switching into the frequency domain. The power spectral density in watt/Hz of the noise voltage is $((|W(f)|^2)/R)$, which for Gaussian white thermal noise is a constant kT and can be pulled out of the equation. The remaining integral disappears since the energy in the matched filter was normalized to unity. Therefore, the SNR is

$$\text{SNR}_{\text{pk out}} = \frac{N\tau P_{\text{echo}}}{kT}. \quad (26)$$

F. Power in Incoherently Processed Signals

In the absence of hardware synchronization and the processing-based synchronization presented here, incoherent summation can be applied. To avoid destructive interference from a lack of phase synchronization, the power in recorded waveforms is summed rather than the complex voltage waveform. Rather than gaining an N^2 increase to the waveform power, incoherent summation only offers a gain of N . The difference between the incoherent and coherent processing begins at $s_2(t)$ because the summation and squaring steps are reversed. After the incoherent summation, the signal would be

$$\begin{aligned} s_2^{\text{incoherent}}(t_{\text{delay}}) &= \sum_{m=1}^N |ae^{j(\phi_m+\phi_b)} e^{-j(\phi_m+\phi_a)} \sqrt{Q}|^2 \\ &= \sum_{m=1}^N |a\sqrt{Q}e^{j(\phi_b-\phi_a)}|^2 \\ &= a^2 N Q \quad (V^2 s). \end{aligned} \quad (27)$$

This subtle difference leads to a processing gain of N rather than N^2

$$s_4^{\text{incoherent}}(t_{\text{delay}}) = \frac{a^2 N E_{\text{TX}}}{\tau} = N P_{\text{echo}} \text{ (Watts)}. \quad (28)$$

G. Incoherent Summation Noise Statistics

We find $\tilde{\sigma}_{\text{noise PW}}$ to evaluate SNR. Following incoherent summation, the noise is represented as

$$\begin{aligned} \sum_{m=1}^N |X_m|^2 + |Y_m|^2 &= \sum_{m=1}^{2N} |Z_m|^2 \\ Z &\sim N(0, \tilde{\sigma}_v^2). \end{aligned} \quad (29)$$

When the standard deviation of the real and imaginary parts of the noise is 1, then this is a chi-squared distribution with $2N$ degrees of freedom (k), a standard deviation of $\sqrt{2k} = \sqrt{4N}$, and a mean of $k = 2N$. The nonunity standard deviation forms the χ^2 distribution stretched by $\tilde{\sigma}_v^2$, τ , and R , scaling the noise power standard deviation to $\tilde{\sigma}_v^2 \sqrt{2k}(1/\tau R) = \tilde{\sigma}_v^2 \sqrt{4N}(1/\tau R)$ and the mean power to $\tilde{\sigma}_v^2 k(1/\tau R) = 2N\tilde{\sigma}_v^2(1/\tau R)$.

H. SNR of Standard Incoherent Processing

Incoherent summation does not satisfy (14), so the SNR definition cannot be reduced to a ratio of average powers. As simulated in Appendix B-I, $((E[|s(t)|^2])/(\tilde{\sigma}_{\text{noise PW}})) \neq ((E[|s(t)|^2])/((E[|n(t)|^2])))$. The incoherently processed noise power has a standard deviation of $2\tilde{\sigma}_v^2 \sqrt{4N}(1/\tau R)$,

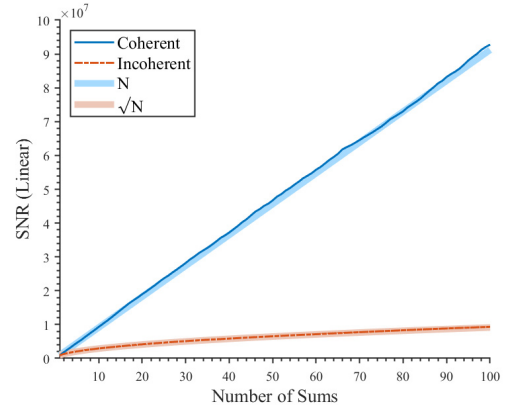


Fig. 18. SNR defined as the ratio of signal power to standard deviation of noise power encapsulates the signal detectability improvement in both summation methods. The coherent summation grows as N and the incoherent summation grows as \sqrt{N} .

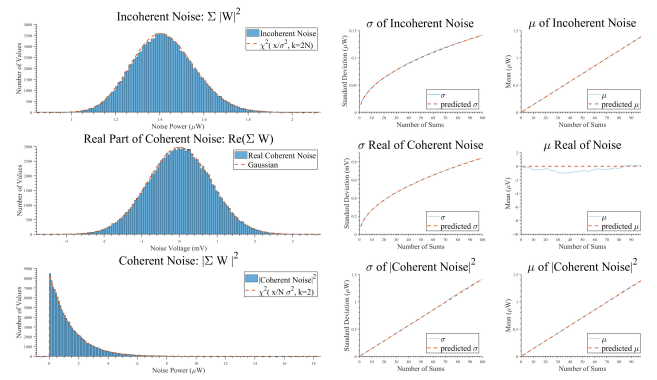


Fig. 19. Noise statistics after N sums for complex white Gaussian noise where both the real and imaginary components have standard deviations equivalent to the standard deviation of the signal. The incoherent summation of noise is accurately represented with a chi-squared distribution where $k = 2N$ and coherent summation follows a chi-squared distribution where $k = 2$ (Rayleigh).

where $\tilde{\sigma}_v^2 = (kTR/2)$ for thermal noise. Therefore, $\tilde{\sigma}_{\text{noise PW}} = (\sqrt{N}kT/\tau)$. The SNR for incoherent summation is

$$\text{SNR}^{\text{incoherent}} = \frac{\sqrt{N}\tau P_{\text{echo}}}{kT}. \quad (30)$$

I. Comparison of SNR Definitions in LFM CW Simulation

The analytical conclusions were checked with a simulation of a complex linear frequency swept continuous chirp generated as $e^{j(\pi s t^2 + 2\pi f_c t)}$ with a bandwidth of 15.36 MHz. Losses were applied to this signal to simulate real data, including antenna gain, geometric spreading, attenuation, and reflection losses for the time-delayed basal reflection and geometric spreading for the direct path. White Gaussian noise was generated with a standard deviation equivalent to the standard deviation of the simulated signal. The results where the signal and noise are kept separate are shown in the following, where using $\text{SNR} = ((E[|v(t)|^2])/(\tilde{\sigma}_{\text{noise PW}}))$ gave the anticipated results with N and \sqrt{N} gains for coherent and incoherent summation, respectively, as shown in Fig. 18. The noise shows the anticipated chi-squared statistics for incoherent and coherent summation (see Fig. 19). The SNR

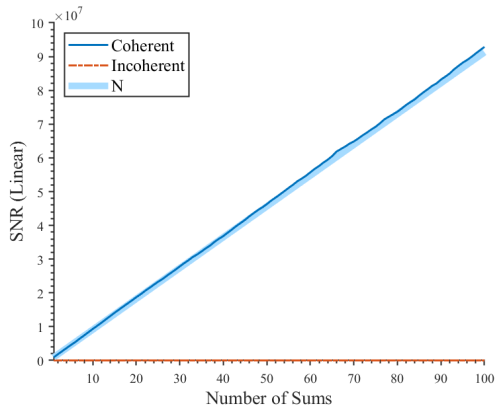


Fig. 20. SNR defined in the traditional manner as average signal power over average noise power results in an incoherent SNR that does not improve with sums, even though the signal becomes more prominent above the noise. In this definition, the coherent summation SNR grows as N and the incoherent summation SNR is constant.

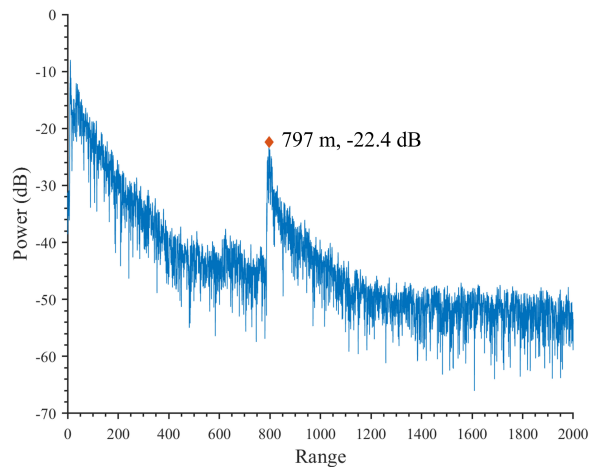


Fig. 21. Ice thickness at 84.24892°S and 153.91115°W, Whillans Ice Stream, West Antarctica was measured to be 797 m thick using an ApRES.

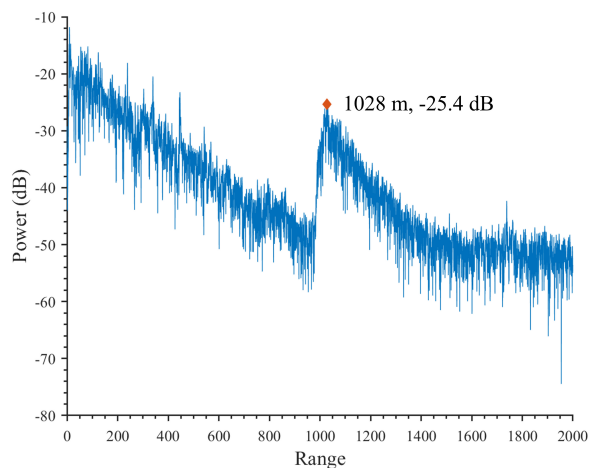


Fig. 22. Ice thickness at Store Glacier, Greenland (near 70.557821°N and 50.091945°W) was measured to be 1028 m thick using an ApRES.

defined as a ratio of average power yields the same coherent summation gain but does not appropriately quantify the improving signal detectability for incoherent summation, as shown in Fig. 20.

APPENDIX C ICE THICKNESS MEASUREMENTS

We obtained our ice thickness measurements at Whillans Ice Stream and Store Glacier using an ApRES [35] at the location of the transmitter. The ice thickness may have varied in the surrounding area, but significant relief is not expected, particularly at the Whillans location where measurements are made over a subglacial lake. The basal reflection at Whillans Ice Stream, shown in Fig. 21, exhibits a very distinct peak, presumably due to the high dielectric contrast between the lake and the ice. In comparison, the basal reflection at Store Glacier crests more slowly (see Fig. 22).

APPENDIX D VARIABLES

The variables used in this article are listed in the Nomenclature.

ACKNOWLEDGMENT

The authors would like to thank Chloe Gustafson for providing fieldwork assistance, Ben Galton-Fenzi and Sue Cook from the Australian Antarctic Division for providing field equipment. Antarctic logistical support was provided by the Antarctic Support Contract, New York Air National Guard, and UNAVCO.

REFERENCES

- [1] D. M. Schroeder *et al.*, “Five decades of radioglaciology,” *Ann. Glaciol.*, vol. 61, no. 81, pp. 1–13, Apr. 2020.
- [2] A. Rutishauser *et al.*, “Discovery of a hypersaline subglacial lake complex beneath Devon Ice Cap, Canadian Arctic,” *Sci. Adv.*, vol. 4, no. 4, p. eaar4353, Apr. 2018.
- [3] T. M. Jordan *et al.*, “A constraint upon the basal water distribution and thermal state of the Greenland Ice Sheet from radar bed echoes,” *Cryosphere*, vol. 12, no. 9, pp. 2831–2854, Sep. 2018.
- [4] W. Chu, D. M. Schroeder, H. Seroussi, T. T. Creyts, and R. E. Bell, “Complex basal thermal transition near the onset of Petermann Glacier, Greenland,” *J. Geophys. Res., Earth Surf.*, vol. 123, no. 5, pp. 985–995, 2018.
- [5] T. M. Jordan, D. M. Schroeder, D. Castelletti, J. Li, and J. Dall, “A polarimetric coherence method to determine ice crystal orientation fabric from radar sounding: Application to the NEEM Ice Core Region,” *IEEE Trans. Geosci. Remote Sens.*, vol. 57, no. 11, pp. 8641–8657, Nov. 2019.
- [6] T. J. Young, C. Martín, P. Christoffersen, D. M. Schroeder, S. M. Tulaczyk, and E. J. Dawson, “Rapid and accurate polarimetric radar measurements of ice crystal fabric orientation at the Western Antarctic Ice Sheet (WAIS) Divide ice core site,” *Cryosphere Discuss.*, vol. 5, no. 8, pp. 1–22, 2020.
- [7] D. M. Schroeder, H. Seroussi, W. Chu, and D. A. Young, “Adaptively constraining radar attenuation and temperature across the Thwaites Glacier catchment using bed echoes,” *J. Glaciol.*, vol. 62, no. 236, pp. 1075–1082, 2016.
- [8] K. Winter *et al.*, “Radar-detected englacial debris in the West Antarctic Ice Sheet,” *Geophys. Res. Lett.*, vol. 46, nos. 17–18, pp. 10454–10462, 2019.
- [9] W. Chu, D. M. Schroeder, and M. Siegfried, “Retrieval of englacial firm aquifer thickness from ice-penetrating radar sounding in Southeastern Greenland,” *Geophys. Res. Lett.*, vol. 45, no. 21, pp. 711–770, 2018.
- [10] J. A. MacGregor, D. P. Winebrenner, H. Conway, K. Matsuoka, P. A. Mayewski, and G. D. Clow, “Modeling englacial radar attenuation at Siple Dome, West Antarctica, using ice chemistry and temperature data,” *J. Geophys. Res.*, vol. 112, no. F3, pp. 1–14, 2007.
- [11] K. Christianson *et al.*, “Basal conditions at the grounding zone of Whillans Ice Stream, West Antarctica, from ice-penetrating radar,” *J. Geophys. Res., Earth Surf.*, vol. 121, no. 11, pp. 1954–1983, Nov. 2016.

- [12] J. MacGregor *et al.*, "A synthesis of the basal thermal state of the Greenland Ice Sheet," *J. Geophys. Res., Earth Surface*, vol. 121, no. 7, pp. 1328–1350, 2016.
- [13] J. A. MacGregor *et al.*, "Radar attenuation and temperature within the Greenland Ice Sheet," *J. Geophys. Res., Earth Surf.*, vol. 120, no. 6, pp. 983–1008, 2015.
- [14] N. Holschuh, D. A. Lilien, and K. Christianson, "Thermal weakening, convergent flow, and vertical heat transport in the Northeast Greenland Ice Stream shear margins," *Geophys. Res. Lett.*, vol. 46, no. 14, pp. 8184–8193, Jul. 2019.
- [15] K. Matsuoka, "Pitfalls in radar diagnosis of ice-sheet bed conditions: Lessons from englacial attenuation models," *Geophys. Res. Lett.*, vol. 38, no. 5, pp. 1–5, Mar. 2011.
- [16] T. J. Young *et al.*, "Resolving the internal and basal geometry of ice masses using imaging phase-sensitive radar," *J. Glaciol.*, vol. 64, no. 246, pp. 649–660, Aug. 2018.
- [17] X. Wu, K. C. Jezek, E. Rodriguez, S. Gogineni, F. Rodriguez-Morales, and A. Freeman, "Ice sheet bed mapping with airborne SAR tomography," *IEEE Trans. Geosci. Remote Sens.*, vol. 49, no. 10, pp. 3791–3802, Oct. 2011.
- [18] L. Improta, A. Zollo, A. Herrero, R. Frattini, J. Virieux, and P. Dell'Aversana, "Seismic imaging of complex structures by non-linear traveltimes inversion of dense wide-angle data: Application to a thrust belt," *Geophys. J. Int.*, vol. 151, no. 1, pp. 264–278, Oct. 2002.
- [19] B. C. Zelt, M. Talwani, and C. A. Zelt, "Prestack depth migration of dense wide-angle seismic data," *Tectonophysics*, vol. 286, nos. 1–4, pp. 193–208, Mar. 1998.
- [20] C. Samson, P. J. Barton, and J. Karwatowski, "Imaging beneath an opaque basaltic layer using densely sampled wide-angle OBS data1," *Geophys. Prospecting*, vol. 43, no. 4, pp. 509–527, May 1995.
- [21] S. Kodaira, N. Takahashi, A. Nakanishi, S. Miura, and Y. Kaneda, "Subducted seamount imaged in the rupture zone of the 1946 Nankaido earthquake," *Science*, vol. 289, no. 5476, pp. 104–106, Jul. 2000.
- [22] J. Suckale, J. D. Platt, T. Perol, and J. R. Rice, "Deformation-induced melting in the margins of the West Antarctic ice streams," *J. Geophys. Res., Earth Surf.*, vol. 119, no. 5, pp. 1004–1025, May 2014.
- [23] C. R. Meyer and B. M. Minchew, "Temperate ice in the shear margins of the Antarctic Ice Sheet: Controlling processes and preliminary locations," *Earth Planet. Sci. Lett.*, vol. 498, pp. 17–26, Sep. 2018.
- [24] R. Drews *et al.*, "Constraining variable density of ice shelves using wide-angle radar measurements," *Cryosphere*, vol. 10, no. 2, pp. 811–823, Apr. 2016.
- [25] T. Murray, A. Booth, and D. M. Rippin, "Water-content of glacier-ice: Limitations on estimates from velocity analysis of surface ground-penetrating radar surveys," *J. Environ. Eng. Geophys.*, vol. 12, no. 1, pp. 87–99, Mar. 2007.
- [26] D. P. Winebrenner, B. E. Smith, G. A. Catania, H. B. Conway, and C. F. Raymond, "Radio-frequency attenuation beneath Siple Dome, West Antarctica, from wide-angle and profiling radar observations," *Ann. Glaciol.*, vol. 37, pp. 226–232, Jan. 2003.
- [27] N. Holschuh, K. Christianson, S. Anandakrishnan, R. B. Alley, and R. W. Jacobel, "Constraining attenuation uncertainty in common midpoint radar surveys of ice sheets," *J. Geophys. Res., Earth Surf.*, vol. 121, no. 10, pp. 1876–1890, Oct. 2016.
- [28] M. Milosevic, "On the nature of the evanescent wave," *Appl. Spectrosc.*, vol. 67, no. 2, pp. 126–131, Feb. 2013.
- [29] M. Segura, S. Niranjayan, H. Hashemi, and A. F. Molisch, "Experimental demonstration of nanosecond-accuracy wireless network synchronization," in *Proc. IEEE Int. Conf. Commun. (ICC)*, Jun. 2015, pp. 6205–6210.
- [30] D. Zachariah, S. Dwivedi, P. Händel, and P. Stoica, "Scalable and passive wireless network clock synchronization in LOS environments," *IEEE Trans. Wireless Commun.*, vol. 16, no. 6, pp. 3536–3546, Jun. 2017.
- [31] M. W. S. Overdick, J. E. Canfield, A. G. Klein, and D. R. Brown, "A software-defined radio implementation of timestamp-free network synchronization," in *Proc. IEEE Int. Conf. Acoust., Speech Signal Process. (ICASSP)*, Mar. 2017, pp. 1193–1197.
- [32] S. Prager, M. S. Haynes, and M. Moghaddam, "Wireless subnanosecond RF synchronization for distributed ultrawideband software-defined radar networks," *IEEE Trans. Microw. Theory Techn.*, vol. 68, no. 11, pp. 4787–4804, Nov. 2020.
- [33] S. Mghabghab, H. Ouassal, and J. A. Nanzer, "Wireless frequency synchronization for coherent distributed antenna arrays," in *Proc. IEEE Int. Symp. Antennas Propag., USNC-URSI Radio Sci. Meeting*, Jul. 2019, pp. 1575–1576.
- [34] M. Younis, R. Metzger, and G. Krieger, "Performance prediction of a phase synchronization link for bistatic SAR," *IEEE Geosci. Remote Sens. Lett.*, vol. 3, no. 3, pp. 429–433, Jul. 2006.
- [35] P. V. Brennan, K. Nicholls, L. B. Lok, and H. Corr, "Phase-sensitive FMCW radar system for high-precision Antarctic ice shelf profile monitoring," *IET Radar, Sonar Navigat.*, vol. 8, no. 7, pp. 776–786, Aug. 2014.
- [36] M. E. Peters, "Analysis techniques for coherent airborne radar sounding: Application to west Antarctic ice streams," *J. Geophys. Res.*, vol. 110, no. B6, pp. 1–17, 2005.
- [37] ANSYS Inc., "Calculating the voltage drop along a line," in *ANSYS HFSS Field Calculator Cookbook*. Canonsburg, PA, USA: ANSYS, Release 17.0, Dec. 2015, pp. 27–28.
- [38] N. Bienert, "Bienert/bistatic_radar_public: V1.0.0," Zenodo, Version 1.0, Stanford Univ., Stanford, CA, USA, Tech. Rep., Oct. 2021, doi: [10.5281/zenodo.5565362](https://doi.org/10.5281/zenodo.5565362).
- [39] N. Bienert *et al.*, "Bistatic radar sounding of Whillans Ice Stream, Antarctica and Store Glacier, Greenland," USAP Data Center, Palisades, NY, USA, Tech. Rep., Sep. 2021, doi: [10.15784/601472](https://doi.org/10.15784/601472).
- [40] C. A. Balanis, *Advanced Engineering Electromagnetics*. Hoboken, NJ, USA: Wiley, 2012.
- [41] A. K. Kendrick *et al.*, "Surface meltwater impounded by seasonal englacial storage in West Greenland," *Geophys. Res. Lett.*, vol. 45, no. 19, pp. 410–474, Oct. 2018.
- [42] L. Carrer, C. Gerekos, F. Bovolo, and L. Bruzzone, "Distributed radar sounder: A novel concept for subsurface investigations using sensors in formation flight," *IEEE Trans. Geosci. Remote Sens.*, vol. 57, no. 12, pp. 9791–9809, Dec. 2019.
- [43] M. S. Haynes *et al.*, "Debris: Distributed element beamformer radar for ice and subsurface sounding," in *Proc. IEEE Int. Geosci. Remote Sens. Symp. (IGARSS)*, Jul. 2021, pp. 651–654.
- [44] E. Mantelli and C. Schoof, "Ice sheet flow with thermally activated sliding. Part 2: The stability of subtemperate regions," *Proc. Roy. Soc. A, Math., Phys. Eng. Sci.*, vol. 475, no. 2231, Nov. 2019, Art. no. 20190411.
- [45] A. Fowler, "A sliding law for glaciers of constant viscosity in the presence of subglacial cavitation," *Proc. Roy. Soc. London A. Math. Phys. Sci.*, vol. 407, no. 1832, pp. 147–170, 1986.
- [46] L. Liboutry, "General theory of subglacial cavitation and sliding of temperate glaciers," *J. Glaciol.*, vol. 7, no. 49, pp. 21–58, 1968.
- [47] W. Chu, D. M. Schroeder, H. Seroussi, T. T. Creyts, S. J. Palmer, and R. E. Bell, "Extensive winter subglacial water storage beneath the Greenland Ice Sheet," *Geophys. Res. Lett.*, vol. 43, no. 24, pp. 412–484, Dec. 2016.
- [48] L. Mony, J. L. Roberts, and J. A. Halpin, "Inferring geothermal heat flux from an ice-borehole temperature profile at Law Dome, East Antarctica," *J. Glaciol.*, vol. 66, no. 257, pp. 509–519, Jun. 2020.
- [49] D. M. Schroeder, D. D. Blankenship, D. A. Young, and E. Quartini, "Evidence for elevated and spatially variable geothermal flux beneath the West Antarctic Ice Sheet," *Proc. Nat. Acad. Sci. USA*, vol. 111, no. 25, pp. 9070–9072, 2014.
- [50] H. Seroussi, E. R. Ivins, D. A. Wiens, and J. Bondzio, "Influence of a West Antarctic mantle plume on ice sheet basal conditions," *J. Geophys. Res., Solid Earth*, vol. 122, no. 9, pp. 7127–7155, Sep. 2017.
- [51] M. Zahn, *Electromagnetic Field Theory: A Problem Solving Approach*. Hoboken, NJ, USA: Wiley, 1979.
- [52] F. Ulaby and R. Umberto, *Fundamentals of Applied Electromagnetics*, 7th ed. Upper Saddle River, NJ, USA: Pearson, 2015.
- [53] D. E. Stillman, J. A. MacGregor, and R. E. Grimm, "The role of acids in electrical conduction through ice," *J. Geophys. Res., Earth Surf.*, vol. 118, no. 1, pp. 1–16, Mar. 2013.
- [54] E. Pettinelli *et al.*, "Dielectric properties of Jovian satellite ice analogs for subsurface radar exploration: A review," *Rev. Geophys.*, vol. 53, no. 3, pp. 593–641, 2015.
- [55] I. G. Cumming and F. H. Wong, *Digital Processing of Synthetic Aperture Radar Data Algorithms and Implementation*. Norwood, MA, USA: Artech House, 2005.
- [56] R. D. Fiete and T. A. Tantal, "Comparison of SNR image quality metrics for remote sensing systems," *Opt. Eng.*, vol. 40, no. 4, pp. 574–585, 2001.
- [57] F. Ulaby and D. Long, *Microwave Radar and Radiometric Remote Sensing*. Norwood, MA, USA: Artech House, 2015.
- [58] R. K. Raney, "Theory of quadratic filters," M.S. thesis, Radar Opt. Lab., Willow Run Lab., Inst. Sci. Technol., Univ. Michigan, Ann Arbor, MI, USA, 1969.

- [59] M. S. Haynes, E. Chapin, and D. M. Schroeder, "Geometric power fall-off in radar sounding," *IEEE Trans. Geosci. Remote Sens.*, vol. 56, no. 11, pp. 6571–6585, Nov. 2018.



Nicole L. Bienert (Member, IEEE) received the B.S. degree (*cum laude*) in electrical engineering, with a minor in physics, from the Schreyers Honors College, Pennsylvania State University, University Park, PA, USA, in 2018, and the M.S.E.E. degree from Stanford University, Stanford, CA, USA, in 2020, where she is currently pursuing the Ph.D. degree in electrical engineering under the supervision of Prof. Dustin M. Schroeder.

As a National Science Foundation Graduate Research Fellow, she currently works with the Radio Glaciology Group on developing novel radar sensing techniques of terrestrial and planetary ice. She is also a Visiting Scholar at the Jet Propulsion Laboratory, Pasadena, CA, USA, where she is investigating beamforming techniques and analyzing the potential performance of a distributed orbital sounder. She has previously been involved in researching resonance radar imaging in 2017, planning antenna testing of NISAR in 2016, and developing an inflatable antenna for CubeSats in 2016 at the Jet Propulsion Laboratory. Her research interests include remote sensing, electromagnetics, radar sounder instrument design, and tomography.



Dustin M. Schroeder (Senior Member, IEEE) received the B.A. degree in physics and the B.S.E.E. degree in electrical engineering from Bucknell University, Lewisburg, PA, USA, both in 2007, and the Ph.D. degree in geophysics from The University of Texas at Austin, Austin, TX, USA, in 2014.

He is currently an Assistant Professor of geophysics and (by courtesy) electrical engineering with Stanford University, Stanford, CA, USA, where he is also a Center Fellow (by courtesy) with the Stanford Woods Institute for the Environment. His research group seeks to approach problems from both an Earth system science and a radar system engineering perspective. He participated in three Antarctic field seasons with the Investigating the Cryospheric Evolution of the Central Antarctic Plate (ICECAP) Project and NASA's Operation Ice Bridge as a Radar Engineer and Operator. His research focuses on advancing the scientific and technical foundations of geophysical ice-penetrating radar and its use in observing and understanding the interaction of ice and water in the solar system. He is primarily interested in the subglacial and englacial conditions of rapidly changing ice sheets and their contribution to global sea-level rise. However, a growing secondary focus of his work is the subsurface exploration of icy moons. He is also interested in the development and application of science-optimized geophysical radar systems.

Dr. Schroeder is a Science Team Member on the REASON instrument on NASA's Europa Clipper Mission and the Mini-RF instrument on NASA's Lunar Reconnaissance Orbiter.



Sean T. Peters (Member, IEEE) received the B.Sc. degree (*cum laude*) in electrical engineering from Rice University, Houston, TX, USA, in 2015, and the M.Sc. degree in electrical engineering from Stanford University, Stanford, CA, USA, in 2017, where he is currently pursuing the Ph.D. degree in electrical engineering with the Department of Geophysics and Electrical Engineering under the supervision of Prof. Dustin M. Schroeder.

As a part of the Radio Glaciology Research Group, he is involved in developing ambient noise radio glaciology with the Radar Systems Development Team, Stanford University.

Mr. Peters received the National Science Foundation Graduate Research Fellowship, the Stanford's Diversifying Academia Recruiting Excellence Doctoral Fellowship, the Stanford Enhancing Diversity in Graduate Education—Science, Technology, Engineering and Mathematics Fellowship, and the Stanford Engineering's Larry and Joan Owen Fellowship.



Emma J. MacKie (Graduate Student Member, IEEE) received the B.A. degree in Earth and planetary sciences from Harvard University, Cambridge, MA, USA, in 2017. She is currently pursuing the Ph.D. degree in geophysics with Stanford University, Stanford, CA, USA, under the supervision of Prof. Dustin M. Schroeder.

As a member of the Stanford Radio Glaciology Group, she uses machine learning techniques to study subglacial conditions and produce geostastical simulations of subglacial topography.

Mr. MacKie is an Achievement Rewards for College Scientists (ARCS) Scholar.



Eliza J. Dawson received the B.S. degree in atmospheric science from the University of Washington, Seattle, WA, USA, in 2018, with a minor in applied mathematics. She is currently pursuing the Ph.D. degree in geophysics with Stanford University, Stanford, CA, USA, under the supervision of Prof. Dustin M. Schroeder.

As part of the Radio Glaciology Group, she works on integrating ice-penetrating radar observations with numerical ice sheet modeling to investigate the role of the basal thermal regime in controlling the rate of flow and mass loss from the Antarctic ice sheet. She is also a National Science Foundation Research Fellow.



Matthew R. Siegfried (Member, IEEE) received the B.A. and M.S. degrees in Earth sciences from the Dartmouth College, Hanover, NH, USA, in 2008 and 2010, respectively, and the Ph.D. degree in geophysics from the Scripps Institution of Oceanography, University of California at San Diego, La Jolla, CA, USA, in 2015.

He is currently an Assistant Professor with the Department of Geophysics and an Affiliate Faculty Member in hydrologic sciences and engineering and humanitarian engineering at the Colorado School of Mines, Golden, CO, USA. His research group at the Mines Glaciology Laboratory uses satellite remote sensing techniques in combination with field-based and airborne geophysical method to understand physical processes of the Earth's cryosphere. He participated in NASA's ICESat-2 mission Science Definition Team and Science Team activities from 2011 to 2020. He is a member of the NASA's final Operation IceBridge Science Team from 2017 to 2020 and the NASA's GNSS Science Team.



Rohan Sanda is currently pursuing the B.S. degree in electrical engineering (with a minor in history) with Stanford University, Stanford, CA, USA.

As a member of the Radio Glaciology Group, Stanford University, he works on advancing the development of passively synchronized bistatic radar configurations to study ice sheets.

Poul Christoffersen, photograph and biography not available at the time of publication.